PCCP

ROYAL SOCIETY OF CHEMISTRY

PAPER

View Article Online
View Journal | View Issue

Cite this: *Phys. Chem. Chem. Phys.*, 2023, **25**, 21245

Probing conformational landscapes of binding and allostery in the SARS-CoV-2 omicron variant complexes using microsecond atomistic simulations and perturbation-based profiling approaches: hidden role of omicron mutations as modulators of allosteric signaling and epistatic relationships†

Gennady Verkhivker, *[abc] Mohammed Alshahrani, [a] Grace Gupta, [a] Sian Xiao [d] and Peng Tao [d]

Received 4th May 2023,
Accepted 2nd August 2023

DOI: 10.1039/d3cp02042h

rsc.li/pccp

In this study, we systematically examine the conformational dynamics, binding and allosteric communications in the Omicron BA.1, BA.2, BA.3 and BA.4/BA.5 spike protein complexes with the ACE2 host receptor using molecular dynamics simulations and perturbation-based network profiling approaches. Microsecond atomistic simulations provided a detailed characterization of the conformational landscapes and revealed the increased thermodynamic stabilization of the BA.2 variant which can be contrasted with the BA.4/BA.5 variants inducing a significant mobility of the complexes. Using the dynamics-based mutational scanning of spike residues, we identified structural stability and binding affinity hotspots in the Omicron complexes. Perturbation response scanning and network-based mutational profiling approaches probed the effect of the Omicron mutations on allosteric interactions and communications in the complexes. The results of this analysis revealed specific roles of Omicron mutations as conformationally plastic and evolutionary adaptable modulators of binding and allostery which are coupled to the major regulatory positions through interaction networks. Through perturbation network scanning of allosteric residue potentials in the Omicron variant complexes performed in the background of the original strain, we characterized regions of epistatic couplings that are centered around the binding affinity hotspots N501Y and Q498R. Our results dissected the vital role of these epistatic centers in regulating protein stability, efficient ACE2 binding and allostery which allows for accumulation of multiple Omicron immune escape mutations at other sites. Through integrative computational approaches, this study provides a systematic analysis of the effects of Omicron mutations on thermodynamics, binding and allosteric signaling in the complexes with ACE2 receptor.

Introduction

The SARS-CoV-2 spike glycoprotein is a key molecule involved in the virus's entry into host cells. It is composed of two subunits, S1 and S2, and is responsible for binding to the host cell surface and for mediating fusion of the viral and cellular membranes.[1–9] The S protein of SARS-CoV-2 has a complex architecture consisting of an amino (N)-terminal S1 subunit that experiences functional motions between the open and closed forms, and a structurally rigid carboxyl (C)-terminal S2 subunit. S1 subunit is comprised of the N-terminal domain (NTD), the receptor-binding domain (RBD), and two structurally conserved subdomains, SD1 and SD2.[10–15] The biophysical

[a] *Keck Center for Science and Engineering, Schmid College of Science and Technology, Chapman University, Orange, CA 92866, USA. E-mail: alshahrani@chapman.edu, grgupta@chapman.edu*
[b] *Department of Biomedical and Pharmaceutical Sciences, Chapman University School of Pharmacy, Irvine, CA 92618, USA. E-mail: verkhivk@chapman.edu; Tel: +1-714-516-4586*
[c] *Department of Pharmacology, Skaggs School of Pharmacy and Pharmaceutical Sciences, University of California San Diego, 9500 Gilman Drive, La Jolla, CA 92093, USA*
[d] *Department of Chemistry, Center for Research Computing, Center for Drug Discovery, Design, and Delivery (CD4), Southern Methodist University, Dallas, Texas, 75275, USA. E-mail: sxiao@smu.edu, ptao@smu.edu*

† Electronic supplementary information (ESI) available. See DOI: https://doi.org/10.1039/d3cp02042h

studies have extensively characterized the thermodynamic and kinetic properties of the SARS-CoV-2 S trimer revealing a complex interplay between subdomain movements and long-range interactions which couple the S1 and S2 subunits to modulate the RBD equilibrium and population-shifts between the RBD open (up) and closed (down) conformations.[16–18] The RBM (Receptor Binding Motif) loop in the RBD is a critical region involved in binding to the ACE2 receptor and is a target for immune recognition by antibodies (Fig. S1, ESI†). The abundance of cryo-EM and X-ray structures of SARS-CoV-2 S variants of concern (VOCs) in various functional states and complexes with antibodies has allowed for an in-depth understanding of molecular mechanisms and binding epitopes that underlie the binding affinity of the S protein with different classes of antibodies.[19–28] The cryo-EM structures of the S Omicron BA.1 variants in different functional states revealed that the dynamic equilibrium between the open and closed S states can induce immune evasion by altering antibody epitopes while simultaneously maintaining structurally stable RBD conformations that allows for the occlusion of highly immunogenic sites.[27,28] The biophysical analysis of protein stability for the Wu-Hu-1, Delta, and Omicron variants using differential scanning fluorimetry (DSF) assay showed that the transition to the folding state for the Omicron BA.1 variant was shifted to the lower temperatures as compared to the Wu-Hu-1 and Delta variants, suggesting a reduced protein stability of the S Omicron BA.1 variant.[29,30] The thermostability of the S-D614G, S-BA.1, and S-BA.2 protein ectodomains evaluated in DSF assays confirmed the reduced stability of the BA.1 protein and greater stability of the BA.2 variant which is still less stable than the original Wu-Hu-1 protein.[31,32] It was also found that the S371L, S373P and S375F Omicron substitutions can promote stabilization of the RBD-up conformation while preventing exposure of other two RBDs to ACE2 binding.[33] Other structural investigations on the Omicron BA.1 variant yielded similar findings, showing that mutations in the Omicron strain tend to enhance both the inter-domain and inter-subunit packing to stabilize 1 RBD-up form of the S protein.[34,35]

Structural studies provided insights into the evolutionary forces driving the development of the Omicron variant by elucidating the thermodynamic factors that influence the interplay between the ACE2 binding affinity and immune escape.[36–40] The cryo-EM study of the S Omicron BA.1 variant examined binding and antigenic properties by bio-layer interferometry showing that most of Omicron modifications (T478K, Q493R, G496S, and Q498R) enhance ACE2 binding while K417N and E484A can decrease the affinity.[41] Atomic force microscopy (AFM) studies quantified the importance of mechanical stability in mediating immune evasion, showing that a combination of mechanical forces, protein stability, and binding interactions play an important role in controlling the virus's fitness advantage and immune escape mechanisms.[42–44]

The Omicron BA.2 subvariants of SARS-CoV-2 have been associated with the increased transmissibility and vaccine evasion capacity.[45,46] Structural and biophysical studies of the RBD-ACE2 complexes for the BA.1.1, BA.2, and BA.3 variants revealed that the binding affinity of the Omicron BA.2 with ACE2 is stronger than the affinities of the BA.3 and BA.1 subvariants.[45] Consistent with these findings, Omicron BA.2 trimer showed a significantly higher ACE2 binding affinity compared to both the S Wu-Hu-1 trimer and the Omicron BA.1 trimer.[46] The surface plasmon resonance (SPR) studies examined binding of the Omicron BA.4/5 RBD showing only a slightly higher binding affinity for ACE2 than the ancestral Wu-Hu-1 strain and the BA.1 variant.[47] The cryo-EM structures and biochemical analysis of the S trimers for BA.1, BA.2, BA.3, and BA.4/BA.5 subvariants demonstrated that the BA.2 variant has a higher binding affinity than the other variants, while the BA.4/BA.5 variants revealed the moderately decreased binding affinity.[48] Other structural studies of the Omicron BA.1, BA.2, BA.2.12.1, BA.4, and BA.5 subvariants confirmed the increased ACE2 binding affinity and a stronger evasion of neutralizing antibody responses for BA.2 as compared to the Wu-Hu-1 and other Omicron sublineages.[49] The structural studies of the S-BA.4/5 binding with human ACE2 (hACE2) and mouse ACE2 (mACE2) showed that N501Y, Q493R, G496S, and Q498R increase the number of interactions with mACE2, while the F486V mutation results in the loss of hydrophobic contacts with hACE2 residues.[50] Several studies examined how Omicron BA.4/BA.5 S variants could affect binding affinity to ACE2 and neutralizing antibodies, showing that a reversion of R493Q and F486V in the BA.4/5 S protein contributes to the increased immune evasion as compared to BA.1 and BA.2.[51–54] At the same time, the L452R mutation in BA.4/BA.5 compensates for the decreased ACE2 binding affinity caused by F486V resulting in the ACE2 binding affinity for BA.4/5 that is comparable to BA.2 variant.[51] Structural studies of the RBD binding with mACE2 showed that the Omicron RBD is adapted to mACE2 better than to hACE2 with mutations Q493R, Q498R and Y505H providing stronger interactions to mACE2.[55]

These studies indicated that Omicron subvariants may have emerged by protecting mutational hotspots that provide strong ACE2 binding while evolving new mutations in the flexible RBD sites to enhance immune evasion potential without compromising ACE2 affinity. Overall, the body of structural-functional studies of the Omicron subvariants revealed that these mutations exerted various impacts on viral molecular characteristics producing a balance of the increased ACE2 binding, the enhanced immune evasion from current antibodies, and the increased replication rates manifesting in rapid virus spread and transmissibiliy.[56]

Computer simulations of the SARS-CoV-2 S proteins have allowed for a better understanding of the molecular mechanisms of viral entry and receptor binding.[57–65] Through simulations, it was revealed that glycosylation plays an important role in modulating the binding of ACE.[57,58] Molecular simulations also provided insights into the conformational changes of the S protein in the viral membrane, as well as its interactions with other viral and cellular components.[57–60] Using computational approaches it was suggested that the S protein could function as an allosteric regulatory machinery controlled by stable allosteric hotspots acting as regulators of spike activity.[66–72]

All-atom MD simulations of the S Omicron trimer and the Omicron RBD–ACE2 complexes revealed that the Omicron mutations may enhance the infectivity of the virus by improving the RBD opening, increasing the binding affinity with ACE2, and optimizing the capacity for antibody escape.[73] MD simulations of the Omicron RBD–ACE2 complexes showed that the K417N and G446S mutations reduce the ACE2 binding affinity due to the introduction of polar residues that disrupt the hydrophobic environment that is necessary for the binding of Omicron RBD and ACE2.[74] On the other hand, the S447N, Q493R, G496S, Q498R, and N501Y mutations were observed to improve the binding affinity with the ACE2 receptor.[74,75]

By combining atomistic MD simulations with mutational scanning and network analysis, our studies revealed that the SARS-CoV-2 S protein can exploit allosteric interactions between structurally stable hotspots of the S2 subunit and dynamic RBD regions to modulate specific regulatory and binding functions.[76,77] The dynamics-based network studies of the S-RBD Delta and Omicron variants showed that a constellation of mutational sites (G496S, Q498R, N501Y and Y505H) form key binding energy hotspots that mediate allosteric communications between S-RBD and ACE2 while other mutational sites could allow for immune evasion at different epitopes.[76] Using the ensemble-based global network analysis, we recently introduced a community-based topological model of the Omicron RBD interactions that characterized functional roles of the Omicron mutational sites in mediating non-additive epistatic effects of mutations.[77] This study demonstrated that non-additive contributions to the binding affinity may be mediated by R493, Y498, and Y501 sites and are greater for the Omicron BA.1.1 and BA.2 complexes that display the strongest ACE2 binding affinity among the Omicron subvariants.[77] A network-based community model for the analysis of epistatic contributions in the Omicron complexes was recently developed revealing the key role of the binding energy hotspots R498 and Y501 in mediating long-range cooperativity with other Omicron sites that creates a complex functional landscape of virus transmissibility.[78] These network-based computational studies suggested allosteric cooperativity between the Omicron mutational sites where the effects of mutations are propagated and can be amplified through a coordinated interaction network that enables modulation of host receptor binding and immune evasion.

In the current study, we expand on this hypothesis and employ a combination of atomistic MD simulations and perturbation profiling approaches to systematically examine and compare the conformational dynamics, binding and allosteric communications in the Omicron BA.1, BA.2, BA.3 and BA.4/BA.5 S-RBD complexes with ACE2. Microsecond atomistic simulations provide a detailed characterization of the conformational landscapes and revealed the increased thermodynamic stabilization of the BA.2 variant which is contrasted with the BA.4/BA.5 variants inducing a significant mobility of the complexes. Using ensemble-based mutational scanning of binding interactions, we characterized binding affinity and structural stability hotspots in the Omicron complexes. Perturbation response scanning and network-based mutational profiling approaches are introduced to probe the effect of the Omicron variants on allosteric communications and characterize roles of Omicron mutations in modulating dynamics, binding and allostery. Perturbation network scanning of allosteric residue potentials performed in the background of the original strain revealed that the key Omicron binding affinity hotspots N501Y and Q498R mediate allosteric interactions and epistatic couplings. Through integrative computational approaches, this study provides a systematic analysis and comparison of the effects of Omicron subvariants BA.1, BA.2, BA.3, and BA.4/BA.5 on conformational dynamics, binding and allosteric signaling in the complexes with the ACE2 receptor. The results suggest a mechanism in which several RBD hotspots that are linked through epistatic couplings may play a significant role in maintaining efficient ACE2 binding and modulating allosteric interactions in the RBD-ACE2 complexes. This may contribute to a compensatory balance between multiple fitness tradeoffs which encompasses viral stability, enhanced transmissibility and the ability of the Omicron variants to accommodate a diverse spectrum of immune-escape mutations compared to earlier variants.

Materials and methods

Structural modeling and refinement

The crystal structures of the BA.1 RBD-hACE2 (pdb id 7WBP),[19] BA.2 RBD-hACE2 (pdb id 7XB0),[45] BA.3 RBD-hACE2 (pdb id 7XB1),[45] and BA.4/BA.5 RBD-hACE2 complexes (pdb id 7XWA)[51] (Fig. 1) were obtained from the Protein Data Bank.[79] During structure preparation stage, protein residues in the crystal structures were inspected for missing residues and protons.

Hydrogen atoms and missing residues were initially added and assigned according to the WHATIF program web interface.[80] The protonation states for all the titratable residues of the ACE2 and RBD proteins were predicted at pH 7.0 using Propka 3.1 software and web server.[81,82]

The missing segments in the studied structures of the SARS-CoV-2 S protein were reconstructed and optimized using template-based loop prediction approach ArchPRED.[83] The side chain rotamers were refined and optimized by SCWRL4 tool.[84] The protein structures were then optimized using atomic-level energy minimization with composite physics and knowledge-based force fields implemented in the 3Drefine method.[85]

All-atom molecular dynamics simulations

The CHARMM36 force field[86] with the TIP3P water model[87] were employed to perform all-atom MD simulations for each of the Omicron RBD-hACE2 complexes. The structures of the SARS-CoV-2 S-RBD complexes were prepared in Visual Molecular Dynamics (VMD 1.9.3).[88] The protein systems were solvated in 130 Å × 85 Å × 75 Å water boxes. In each system, sodium and chloride ions were added to maintain an ionic strength of 0.1 M. The energy minimization was first performed for 10 000 steps with hydrogen bonds constrained and respective protein

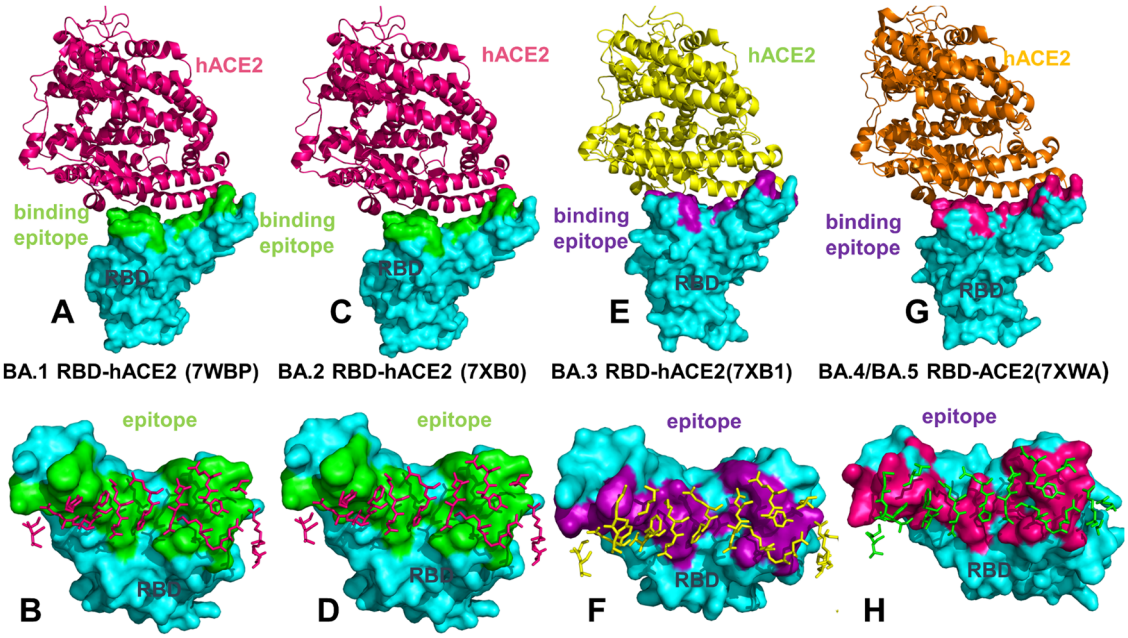

Fig. 1 Structural organization and binding epitopes of the SARS-CoV-2-RBD Omicron complexes with human ACE enzyme. (A) The structure of the Omicron RBD BA.1-ACE2 complex (pdb id 7WBP). The RBD is in cyan surface and ACE2 is in pink ribbons. (B) The RBD-BA.1 binding epitope residues are shown in green surface. The ACE2 binding residues are shown in pink sticks. (C) The structure of the Omicron RBD BA.2-ACE2 complex (pdb id 7XB0). The RBD is in cyan surface and the ACE2 is in pink ribbons. (D) The RBD-BA.2 binding epitope residues are highlighted in green surface. The ACE2 binding residues are shown in pink sticks. (E) The structure of the Omicron RBD BA.3-ACE2 complex (pdb id 7XB1). The RBD is in cyan surface and the ACE2 is in green ribbons. (F) The RBD-BA.2 binding epitope residues are highlighted in purple surface and the ACE2 binding residues are shown in green sticks. (G) The structure of the Omicron RBD BA.4/BA.5-ACE2 complex (pdb id 7XWA). The RBD is shown in cyan surface and the ACE2 is in orange ribbons. (H) The RBD-BA.4/BA.5 binding epitope is shown in dark-pink surface and the ACE2 binding residues are shown in green sticks.

atoms fixed. In the second stage, minimization was performed for 10 000 steps with all protein backbone atoms fixed and an additional 10 000 steps without any constraints.[89]

After energy minimization, the systems were first heated up from 100 to 300 K with a temperature increment of 20 K per 50 picoseconds (ps). Consequently, the systems were subjected to 1.5 nanoseconds (ns) isothermal–isobaric (*NPT*) equilibrations at 300 K (equilibrium run), followed by 1 microsecond (μs) of *NVT* simulations (production run) at 300 K. Snapshots of the production run were saved every 100 ps. In all simulations, the SHAKE constraint was used to constrain bonds associated with hydrogen atoms in the solvent molecules and the proteins.[90] The nonbonding interactions within 10 Å were calculated explicitly. The Lennard-Jones interactions were smoothed out to zero at 12 Å. The long-range electrostatic interactions were calculated using the particle mesh Ewald method[91] with a cut-off of 1.0 nm and a fourth order (cubic) interpolation. The simulations were conducted using OpenMM (version 7.6.0).[92] For each system, MD simulations were conducted three times in parallel to obtain comprehensive sampling. Each individual simulation of the studied systems BA.1 RBD-hACE2, BA.2 RBD-hACE2, BA.3 RBD-hACE2 and BA.4/BA.5 RBD-hACE2 complexes stored 10 000 frames, thus we collected 30 000 frames for each of the complexes. While the production stage of MD simulations is often performed under the *NPT* ensemble to enable a more accurate comparison with the experimental data, the *NPT* ensemble often needs significantly longer time to reach convergence because both temperature and volume fluctuate during the simulations, especially for large systems like SARS-CoV-2 spike glycoprotein complexes. In the current study, we employed an alternative and widely used approach in which the equilibration simulations are conducted in the *NPT* ensemble to allow the total energy and volume of the system fluctuate to reach conditions suitable for the target pressure. This alternative protocol takes advantage of the *NVT* ensemble for better convergence than the *NPT* ensemble given the same length of simulations. A detailed comparison of MD simulations using different force fields and ensembles (including NAMD with the CHARMM36 force field and *NVT* for the production phase) produced models and equilibrium ensembles that are in similar agreement with experimental results.[89]

The root mean square deviations (RMSD) between the reference state and a trajectory of conformations were computed using MDTraj Python library[93,94] and MDAnalysis Python toolkit (**https://www.mdanalysis.org**) utilizing the fast QCP algorithm:[95,96]

$$\mathrm{RMSD}(\mathbf{x}, \mathbf{x}^{\mathrm{ref}}) = \sqrt{\frac{1}{n}\sum_{i=1}^{n} \left|\mathbf{x}_i - \mathbf{x}_i^{\mathrm{ref}}\right|^2} \quad (1)$$

Both tools yielded similar results and we report RMSD values from the MDTraj calculations. The root-mean-square-fluctuation (RMSF) is calculated according to the equation below, where $\mathbf{R}_i$ is

the mean atomic coordinate of the ith C_α atom and $\mathbf{R}_i$ is its instantaneous coordinate:

$$\rho_i = \sqrt{\left\langle (\mathbf{R}_i - \langle \mathbf{R}_i \rangle)^2 \right\rangle} \quad (2)$$

The RMSF analysis and structural changes. By analyzing the trajectories of the system, we also calculate the dynamic correlation between all atoms within the molecule. This dynamic cross-correlation (DCC) between the ith and jth atoms is defined by the following equation:

$$C_{ij} = \frac{\langle \Delta r_i \cdot \Delta r_j \rangle}{\sqrt{\langle \Delta r_i^2 \rangle} \cdot \sqrt{\langle \Delta r_j^2 \rangle}} \quad (3)$$

with Δr_i the displacement from the average position of atom i, and $\langle\rangle$ the time average over the whole trajectory.[97] The DCC values are calculated between -1 and 1, where 1 corresponds to complete correlation, -1 to complete anti-correlation; and 0 indicated no correlation. The generated DCC heatmap between the C_α atoms of selected frames in a trajectory is used to identify dynamic couplings and collective motions in the protein system.

Mutational scanning and sensitivity analysis

We conducted mutational scanning analysis of the binding epitope residues for the SARS-CoV-2 RBD-ACE2 complexes. In the context of RBD-ACE2 complexes, the binding epitope residues refer to the specific amino acid residues within the RBD and the ACE2 receptor that directly interact with each other during the binding process. The binding epitope residues typically include those in the RBD that directly contact the ACE2 receptor and *vice versa*. These residues are crucial for establishing the specific protein–protein interactions that allow the virus to attach to the host cell and initiate infection. BeAtMuSiC approach[98] was employed that is based on statistical potentials describing the pairwise inter-residue distances, backbone torsion angles and solvent accessibilities, and considers the effect of the mutation on the strength of the interactions at the interface and on the overall stability of the complex. In this approach, the binding interface residues are defined based on the condition that the difference between a residue's solvent accessibility in the complex and apo-protein is at least 5%.[98] The solvent accessibility is defined as the ratio of the solvent-accessible surface in the considered structure relative to an extended tripeptide Gly-X-Gly.[99] Each binding epitope residue was systematically mutated using all substitutions and corresponding protein stability and binding free energy changes were computed. We employed rapid calculations based on statistical potentials to compute the ensemble-averaged binding free energy changes using equilibrium samples from simulation trajectories. The binding free energy changes were computed by averaging the results over 1000 equilibrium samples that were evenly distributed along each of the three independent MD simulations for each of the studied systems. Hence, a total of 3000 protein snapshots were employed in the computations of the mutation-induced binding free energies for each of the studied system.

Perturbation response scanning

The Perturbation Response Scanning (PRS) approach[100–102] is a method used to estimate the response of individual residues in a protein system to external forces systematically applied to each residue. PRS performs a residue-by-residue scanning of the initial conformation, by exerting multiple factious external forces of both random direction and magnitude on each residue in the protein structure. After external force perturbation, the subset of residues/forces that invoke a conformational change closest to the target structure are recorded. The PRS analysis was done using ProDy open-source Python software package for protein dynamics analysis.[103] The implemented approach quantifies how perturbations in one region of the protein can propagate and affect the functional movements of other regions and follows a protocol originally proposed by Bahar and colleagues.[104,105] and detailed in our previous studies.[106]

The PRS approach utilizes $3N \times 3N$ Hessian matrix $\boldsymbol{H}$ where N represents the number of residues in the protein. The elements of the Hessian matrix represent the second derivatives of the potential energy at the local minimum and are obtained from MD simulation trajectories for each protein structure, with residues represented by C_α atoms and the deviation of each residue from an average structure was calculated by $\Delta\mathbf{R}_j(t) = \mathbf{R}_j(t) - \mathbf{R}_j(t)$, and corresponding covariance matrix C was then calculated by $\Delta\mathbf{R}\Delta\mathbf{R}^T$. The $3N$-dimensional vector $\Delta\mathbf{R}$ of node displacements in response to $3N$-dimensional perturbation force follows Hooke's law $\boldsymbol{F} = \boldsymbol{H} \times \Delta\mathbf{R}$ connecting the perturbation forces applied to the protein residues to the resulting displacements of the residues. In the PRS implementation, a perturbation force is applied to one residue at a time. The response of the protein system is measured by the displacement vector $\Delta\mathbf{R}^i = \boldsymbol{H}^{-1}\boldsymbol{F}^{(i)}$ which represents the changes in the positions of the residues due to the applied force. In the present implementation, each residue in the S protein structures is sequentially perturbed by applying a total of 250 random forces to each residue. These random forces mimic a sphere of randomly selected directions. Using the residue displacements upon multiple external force perturbations, the magnitude of the response of residue k can be computed as $\langle \|\Delta\mathbf{R}_k^{(i)}\|^2 \rangle$ by averaging over multiple perturbation forces $\mathbf{F}^{(i)}$ thus yielding the ikth element of the $N \times N$ PRS matrix. The average effect of the perturbed effector site i on all other residues is computed by averaging over all sensors (receivers) residues j and can be expressed as $(\Delta\mathbf{R}^i)_{\text{effector}}{}^2$. In turn, the jth column of the PRS matrix describes the sensitivity profile of sensor residue j in response to perturbations of all residues and its average is expressed as $(\Delta\mathbf{R}^i)_{\text{sensor}}{}^2$.

Dynamic network modeling

A graph-based representation of protein structures[107,108] is used to represent residues as network nodes and the inter-residue edges to describe non-covalent residue interactions. The weights of the network edges in the residue interaction networks are determined by dynamic residue cross-correlations

obtained from MD simulations[109] and coevolutionary couplings between residues measured by the mutual information scores.[110] Residue Interaction Network Generator (RING) program[111–113] was employed for generation of the initial residue interaction networks. The edge lengths in the network are then adjusted using the generalized correlation coefficients associated with the dynamic correlation and mutual information shared by each pair of residues. Network edges are weighted for residue pairs within at least one independent simulation. Network analysis was performed using the python package NetworkX.[114]

The short path betweenness of residue i is defined to be the sum of the fraction of shortest paths between all pairs of residues that pass through residue i:

$$C_b(n_i) = \sum_{j<k}^{N} \frac{g_{jk}(i)}{g_{jk}} \quad (4)$$

where g_{jk} denotes the number of shortest geodesics paths connecting j and k, and $g_{jk}(i)$ is the number of shortest paths between residues j and k passing through the node n_i. Residues with high occurrence in the shortest paths connecting all residue pairs have a higher betweenness values. For each node n, the betweenness value is normalized by the number of node pairs excluding n given as $(N-1)(N-2)/2$, where N is the total number of nodes in the connected component that node n belongs to.

Network-based mutational profiling of allosteric residue potentials and epistasis

By applying mutations of protein residues, we compute dynamic couplings of residues and changes in the short path betweenness centrality (SPC), and the average short path length (ASPL) averaged over all modifications in a given position. The details of this approach were described in our recent studies[72,77,78] Here, we briefly outlined the key elements of this approach. The change of SPC or ASPL upon mutational changes of each node is done by systematically removing nodes from the network.

$$\Delta L_i = \langle \| \Delta L_i^{\text{node}}(j) \|^2 \rangle \quad (5)$$

where i is a given site, j is a mutation and $\langle \cdots \rangle$ denotes averaging over mutations. $\Delta L_i^{\text{node}}(j)$ describes the change of SPC or ASPL parameters upon mutation j in a residue node i. ΔL_i is the average change of ASPL triggered by mutational changes in position i.

Z-Score is then calculated for each node as follows:[115,116]

$$Z_i = \frac{\Delta L_i - \langle \Delta L \rangle}{\sigma} \quad (6)$$

$\langle \Delta L \rangle$ is the change of the SPC or ASPL network parameters under mutational scanning averaged over all protein residues in the S-RBD and σ is the corresponding standard deviation. The ensemble-averaged Z score changes are computed from network analysis of the conformational ensembles using 10 000 snapshots of the simulation trajectory. Through this approach, we evaluate the effect of mutations in the RBD residues on long-range allosteric couplings with the other residues in the RBD-ACE2 complex. We used a measurement based on the Jensen-Shannon divergence (JS) for measuring the similarity between the two distributions of mutation-induced ASPL changes in the Omicron variants relative to the Wu-Hu-1 strain. Given two distributions, p and q, both with g categories, the Kullback–Leibler (KL) divergence is defined as follows:

$$\mathrm{KL}(p \parallel q) = \sum_{i=1}^{g} p_g \log \frac{p_g}{q_g} \quad (7)$$

Given two distributions, p and q, both with g categories, the JS divergence is defined as follows:

$$\mathrm{JS}(p,q) = 0.5\mathrm{KL}\left(p \parallel \frac{p+q}{2}\right) + 0.5\mathrm{KL}\left(q \parallel \frac{p+q}{2}\right) \quad (8)$$

Results

Microsecond MD simulations of the omicron RBD-ACE2 complexes reveal distinct dynamic signatures of stable BA.2 RBD and highly mobile BA.4/BA.5 RBD proteins

Mutational landscape of the Omicron subvariants is characterized by a considerable diversity (Table 1). Nonetheless, structural analysis of the RBD complexes with ACE2 for BA.1 (Fig. 1A and B) BA.2 (Fig. 1C and D) BA.3 (Fig. 1E and F) and BA.4/BA.5 complexes (Fig. 1G and H) revealed highly similar RBD conformations, the same binding mode of interactions with the host receptor and virtually identical topography of the binding interface.

To characterize conformational landscapes and dynamic signatures of the Omicron variants, we conducted several independent microsecond MD simulations of the RBD-ACE2 complexes (Fig. 2 and 3). Despite structural similarities between the RBD-ACE2 complexes, we found that the Omicron mutations may lead to distinct dynamic profiles in the BA.2 and BA.4/BA.5 RBDs (Fig. 2). Moreover, Omicron mutations affect conformational dynamics not only through locally induced

Table 1 Mutational landscape of the Omicron subvariants in the S-RBD

Omicron variant	Mutational landscape
BA.1	G339D, S371L, S373P, S375F, K417N, N440K, G446S, S477N, T478K, E484A, Q493R, G496S, Q498R, N501Y, Y505H
BA.2	G339D, S371F, S373P, S375F, T376A, D405N, R408S, K417N, N440K, S477N, T478K, E484A, Q493R, Q498R, N501Y, Y505H
BA.3	G339D, S371F, S373P, S375F, D405N, K417N, N440K, G446S, S477N, T478K, E484A, Q493R, Q498R, N501Y, Y505H
BA.4/BA.5	G339D, S371F, S373P, S375F, T376A, D405N, R408S,K417N, N440K, L452R, S477N, T478K, E484A, F486V, R493Q reversal, Q498R, N501Y, Y505H

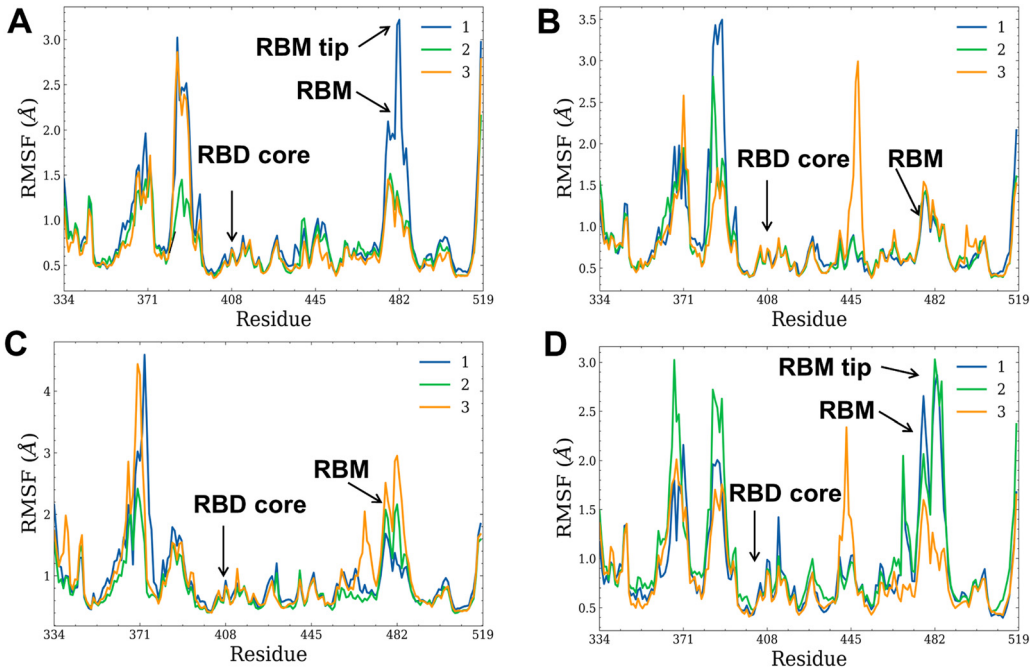

Fig. 2 Conformational dynamics profiles obtained from all-atom MD simulations of the Omicron RBD BA.1, BA.2, BA.3 and BA.4/BA.5 complexes with hACE2. The RMSF profiles for the RBD residues obtained from 3 microsecond MD simulations of the Omicron RBD BA.1-hACE2 complex, pdb id 7WBP (A), Omicron RBD BA.2-hACE2 complex, pdb id 7XB0 (B), Omicron RBD BA.3-hACE2 complex, pdb id 7XB1 (C) and Omicron RBD BA.4/BA.5-hACE2 complex, pdb id 7XWA (D). The RBD core region, RBM motif and RBM tip residues are indicated by arrows on panels (A)–(D).

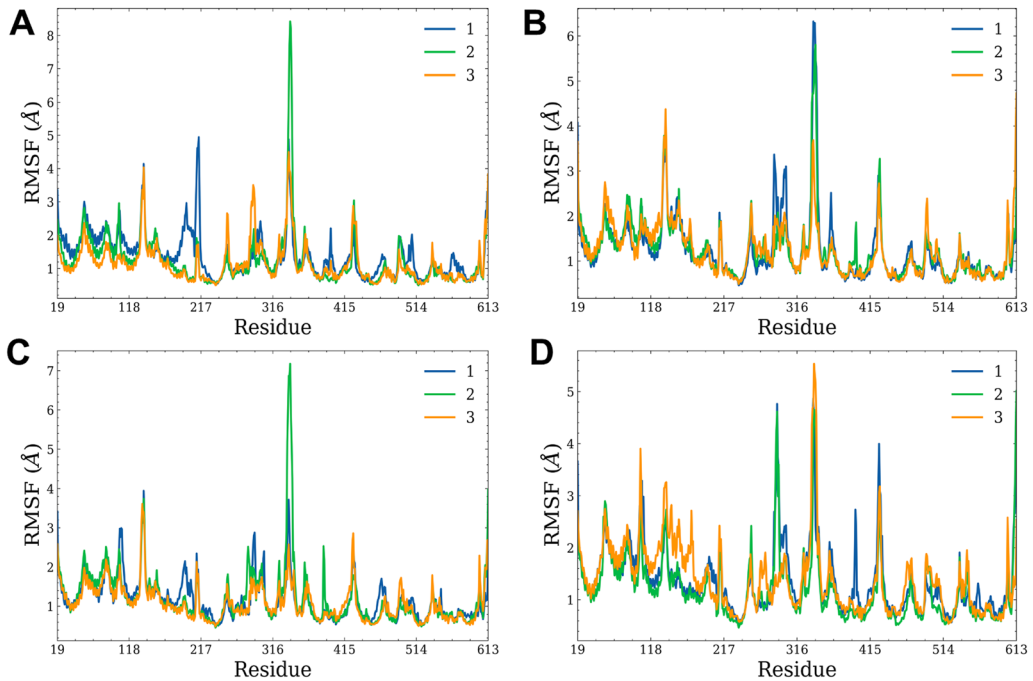

Fig. 3 Conformational dynamics profiles of the ACE2 residues obtained from MD simulations of the Omicron RBD BA.1, BA.2, BA.3 and BA.4/BA.5 complexes with hACE2. The RMSF profiles for the ACE2 residues obtained from 3 microsecond MD simulations of the Omicron RBD BA.1-hACE2 complex, pdb id 7WBP (A), Omicron RBD BA.2-hACE2 complex, pdb id 7XB0 (B), Omicron RBD BA.3-hACE2 complex, pdb id 7XB1 (C) and Omicron RBD BA.4/BA.5-hACE2 complex, pdb id 7XWA (D).

changes but could also induce distinct protein responses over long-range (Fig. 2) (Table 2).

The conformational flexibility of the Omicron RBD was analyzed by calculating the RMSD values (Fig. S2 and S3, ESI†)

Table 2 Structures of the Omicron RBD-hACE2 complexes examined in this study

PDB	System	Per simulation	# Simulations
7WBP	Omicron RBD BA.1-hACE2	1 μs	3
7XB0	Omicron RBD BA.2-hACE2	1 μs	3
7XB1	Omicron RBD BA.3-hACE2	1 μs	3
7XWA	Omicron RBD BA.4/BA.5-hACE2	1 μs	3

and the RMSF distributions for the protein residues (Fig. 2A). The RMSD profiles for the RBD residues reflected convergence of the MD trajectories, particularly for the BA.2, BA.3 an BA.4/BA.5 complexes where two out of three trajectories reached the equilibrium after about 500–600 ns of simulation (Fig. S2B–D, ESI†). A more heterogeneous character of the MD trajectories for the BA.1 complex (Fig. S2A, ESI†) manifested in larger departures from the crystal structure where several trajectories started to show steady fluctuations after 800 ns. The RMSD evolution of the ACE2 residues similarly showed more heterogeneity and greater departures from the crystallographic conformations in the BA.1 and BA.4/BA.5 complexes, while smaller deviations from the experimental structures in the BA.2 and BA.3 complexes (Fig. S3, ESI†). The five-stranded antiparallel β-sheet in the RBD (residues 350–360, 375–380, 394–403) and the interfacial RBD positions (residues 440–456 and 490–505 of the binding interface) showed small RMSF fluctuations (Fig. 2A). These regions of high structural stability were also seen in our earlier simulation studies of the RBD Wu-Hu-1 and Omicron complexes,[76,77] further confirming that these segments remain mostly rigid across all examined RBD complexes with hACE2. The RBM region in the RBD is the intrinsically flexible region that modulates differential binding with the ACE2 receptor and antibodies (Fig. S1, ESI†). We observed the differential mobility of the flexible RBM regions (residues 475–490) which ranges from marked stabilization of these residues in the BA.2 RBD (Fig. 2B) to the increased mobility in the BA.4/BA.5 variants (Fig. 2D). In all complexes, the conformational dynamics profiles revealed the stability of the hydrophobic core regions including F400, I402, F490, Y453, L455, A475, and Y489 residues (Fig. 2). These residues form a network of hydrophobic interactions that play a vital role in the recognition and binding of ACE2 receptors. Conformational fluctuations of the RBD core and interfacial RBD residues were significantly restricted in the Omicron complexes. The trajectories also highlighted the stability of important intermolecular interactions including hydrogen bonds formed by S19 of hACE2 with A475 and N477 of RBD as well as Q24 of hACE2 with N487 of RBD (Tables S1, S2 and Fig. 2 and 3, ESI†). Among important stabilizing interactions preserved in simulations are salt bridges between E35 of hACE2 and R493 from RBD in the BA.1, BA.2 and BA.3 complexes. The stability of these interfacial contacts in simulations are consistent with the key role of these contacts in the binding affinity of the Omicron RBD-ACE2 complexes shown experimentally.[19]

The crucial difference in the dynamic signatures was a considerable stabilization of the RBD in the BA.2 complex (Fig. 2B) and BA.3 complex (Fig. 2C) as opposed to BA.1 and BA.4/BA.5.

In the BA.2 complex, all three MD trajectories displayed a striking reduction in the mobility of the intrinsically flexible RBM loop. Only one of the microsecond trajectories exhibited larger fluctuations (Fig. 2B). MD trajectories of the BA.2 RBD-ACE2 complex showed a considerable degree of convergence in the RMSF values that remained small for the RBD core (RMSF < 1.0 Å) as well as the RBM regions (RMSF < 1.5 Å) including the curtailed fluctuations of the Omicron RBM positions S477N, T478K. The flexibility of the RBM residues was also curtailed in the BA.3 complex in which two trajectories yielded RMSF < 2.5 Å for this region (Fig. 2C). At the same time, the flexibility of the RBM region (residues 475–490) increased in BA.1 (Fig. 2A) and especially BA.4/BA.5 (Fig. 2D). In the BA.4/BA.5 RBD-ACE2 complex, the RBD core residues also showed greater mobility, with some additional local mobility peaks seen for the residues 410–420, 440–450, 470–475. The conformational ensembles revealed that the RBM tip in the BA.2 RBD-ACE2 complex is maintained in a stable fold conformation that can be described as a hook-like folded RBD tip and is similar to the crystallographic conformations. Interestingly, in the BA.1 and especially in a more flexible BA.4/BA.5 RBD, the RBD tip becomes more flexible and often moves away from the "hook" conformation to a more dynamic state in which the RBD tip circulates between a variety of partly disordered conformations. A partly disordered RBM tip can be observed in the BA.4/BA.5 RBD-ACE2 conformations which is reflected in the appreciably increased RMSFs for this system (Fig. 2D). Our analysis also showed that the BA.2 RBD/hACE2 binding interface has the largest number of highly stable intermolecular contacts and hydrogen bonds (Tables S1 and S2, ESI†).

The RMSF analysis of the ACE2 residues showed similar profiles across all the examined variants (Fig. 3). The highly stable ACE2 residues corresponding to the rigid core and the binding interface positions centered around K353 and H34 (Fig. 3). The key ACE2 binding motifs correspond to an alpha-helix (residues 24–31) and a beta-sheet (residue 350–356) that display moderate RMSF values in all complexes. The important polar/charged residue interactions at the interface are formed with ACE2 residues D30, K31, H34 and E35 that display small thermal fluctuations. Other ACE2 residues Q24, M82, Y83, D38, Y41, N330, K353 that anchor various parts of the RBD-ACE2 binding interface remained stable in all MD trajectories (Fig. 3).

To further examine the character of dynamic couplings and quantify correlations between motions of the RBD regions we performed the dynamic cross correlation (DCC) residue analysis and reported the DCC maps for the Omicron RBD-ACE2 complexes (Fig. 4). The DCC maps demonstrated subtle but crucial differences in the dynamic couplings, particularly stronger positive dynamic correlations in the RBD core regions (residues 333–445) for BA.2 (Fig. 4B) and BA.3 (Fig. 4C).

Interestingly, we noticed the presence of negative cross-correlation between motions of the RBM tip (residues 475–485) and other RBD regions (residues 400–470, 490–520) (Fig. 4B). This reflects a more stable RBD in the BA.2 complex yielding

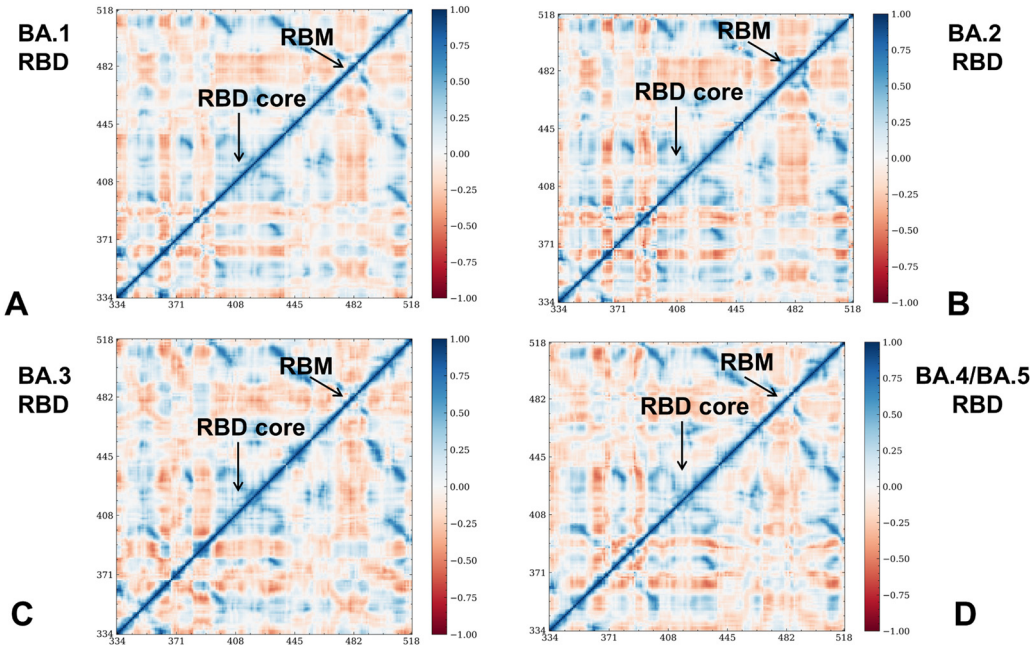

Fig. 4 The DCC for the RBD residues in the Omicron RBD BA.1-hACE2 complex, pdb id 7WBP (A), Omicron RBD BA.2-hACE2 complex, pdb id 7XB0 (B), Omicron RBD BA.3-hACE2 complex, pdb id 7XB1 (C), and Omicron RBD BA.4/BA.5-hACE2 complex, pdb id 7XWA (D). The RBD core region, RBM motif and RBM tip residues are indicated by arrows.

strong dynamic couplings between the RBD core and various parts of the binding interface. A weaker but similar pattern of the inter-correlated motions was also seen in the BA.1 and BA.3 complexes (Fig. 4A and C). Consistent with the conformational dynamics analysis, we found that the correlated motions become appreciably weaker in the BA.4/BA.5 RBD-ACE2 complex (Fig. 4D), reflecting the elevated level of mobility in the RBM region and the increased thermal fluctuations in the RBD core.

To summarize, we found evidence of distinct dynamic patterns in the structurally similar complex conformations. Consistent with the experimental data, our results showed that BA.2 mutations may induce the increased stabilization of the RBD in the complex with ACE2 which may be directly linked with the higher binding affinity, while a considerably greater flexibility may be the important dynamic attribute of the BA.4/BA.5 variants that have the decreased binding affinity.[48] Furthermore, the recent experiments demonstrated that BA.4/BA.5 variants escaped both the vaccine-induced and BA.1 infection-induced antibodies more than BA.1 and BA.2 sublineages.[47] The experimentally observed distinct antigenic profiles for BA.1, BA.2 and BA.5 subvariants[117] may be linked to their distinct dynamic signatures where the increased immune escape of BA.4/BA.5 variant could be enabled by the elevated mobility of the BA.4/BA.5 RBD protein.

Mutational sensitivity analysis identifies structural stability and binding affinity hotspots in the omicron RBD-ACE2 complexes

In silico mutational scanning of the interfacial RBD residues was done using BeAtMuSiC approach[98] that demonstrated high accuracy in several independent benchmark studies of both protein stability and binding affinity.[118,119] Structure-based comparisons of BeAtMuSiC approach with more rigorous, physics-based FoldX[120] and Rosetta approaches[121] showed similar differentiation of stabilizing and destabilizing mutations as well as robust agreement with the experimental stability and binding affinity energies. To provide a systematic comparison, we constructed mutational heatmaps for the RBD interface residues in each of the studied Omicron RBD-hACE2 complexes (Fig. 5). Consistent with deep mutagenesis experiments[122,123] the binding energy hotspots correspond to hydrophobic residues F456, F486, Y489 and Y501 that play a decisive role in binding for Omicron BA.1 (Fig. 5A) and BA.2 complexes (Fig. 5B).

Mutational heatmaps clearly showed that all substitutions in these key interfacial positions can incur a consistent and considerable loss in the stability and binding affinity with ACE2. According to the mutational heatmaps, Y489 and Y501 mutational positions correspond to the key energetic binding hotspots as all mutations in these positions induce significant destabilization changes (Fig. 5A and B). The heatmaps highlighted several other RBD energetic hotspots such as Y453 and F456 that are less prominent that Y489/Y501 but also contribute significantly to the RBD stability and ACE2 binding (Fig. 5A and B). At the same time, mutational scanning of R493 and R498 positions typically yielded moderate destabilization changes as these sites are less sensitive to perturbations than Y489 and Y501 hotspots. It should be noticed that the Omicron RBD BA.2 complex featured a larger binding interface as compared to the BA.1 complex in which the mutation-induced destabilization is distributed over more residues (Fig. 5C and D).

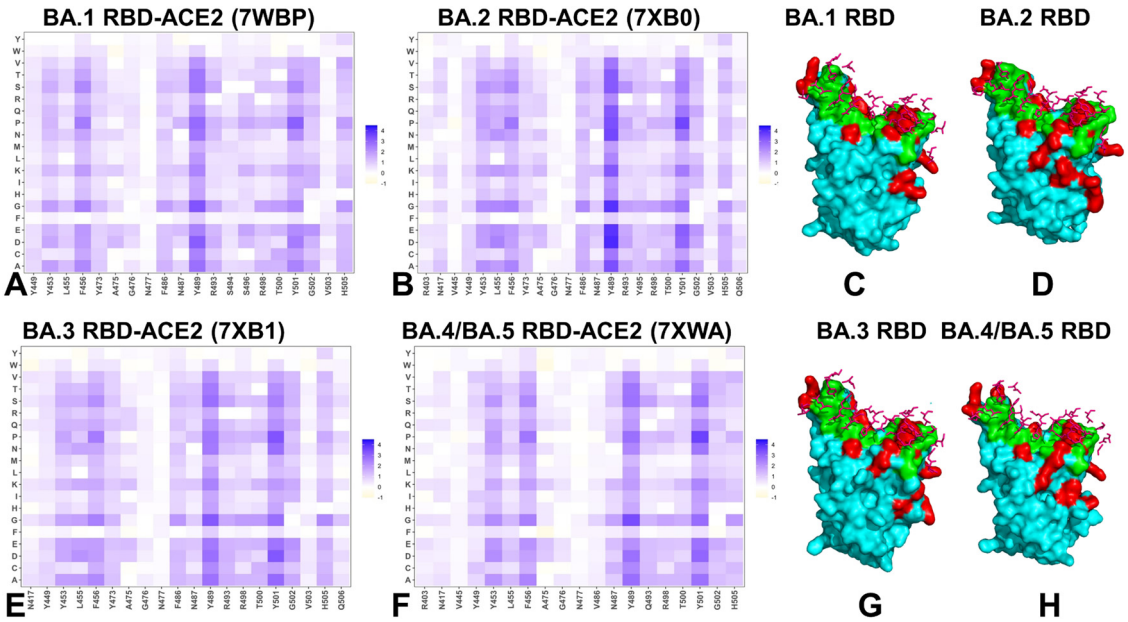

Fig. 5 Mutational profiling of the RBD intermolecular interfaces in the Omicron RBD-hACE2 complexes. The mutational scanning heatmaps are shown for the interfacial RBD residues in the Omicron BA.1 RBD-hACE2 (A), Omicron BA.2 RBD-hACE2 complexes (B), Omicron BA.3 RBD-hACE2 (E) and Omicron BA.4/BA.5 RBD-hACE2 complexes (F). Structural mapping of the RBD binding epitopes of the Omicron BA.1-hACE2 complex (C), BA.2 RBD-hACE2 (D), BA.3 RBD-hACE2 (G) and BA.4/BA.5 RBD-hACE2 (H). The RBD binding epitope is shown in green-colored surface. The Omicron RBD mutational sites are shown in red surface. The ACE2 binding residues are in pink sticks. The standard errors of the mean for binding free energy changes and are within ~0.07–0.18 kcal mol^{-1} using averages based on a total of 3,000 samples obtained from the three MD trajectories for each system.

The difference between the BA.2 RBD and the BA.1 RBD is that BA.2 contains S371F, T376A, D405N, and R408S mutations, whereas BA.1 contains the G446S and G496S mutations. Interestingly, among these mutations, only the G496S mutation is in the RBD-ACE2 interface. The binding interface position S496 in BA.1 is tolerant to mutational changes, producing only moderate destabilization changes ($\Delta\Delta G$ = 0.5–0.7 kcal mol^{-1}) (Fig. 5A). Despite a larger binding interface in BA.2 which featured R403, V445 and G446 residues, these positions are tolerant to perturbations and cause only modest destabilization (Fig. 5B). MD simulations showed that BA.2 RBD with G446/G496 was more stable than BA.1 RBD with S446/S496. It appeared that the hydrogen bond interactions between ACE2 D38 and RBD residues R498/Y449 may be weakened in the presence of S496 for the BA.1 RBD. This may also contribute to the experimentally observed stronger binding affinity of the BA.2 RBD-ACE2 as compared to the BA.1 RBD-ACE2 complex.[45]

Mutational scanning analysis revealed that the binding energy hotspots Y453, L455, F456, Y489, and Y501 are shared between BA.2 (Fig. 5B) and BA.3 complexes (Fig. 5E), while the interfacial positions A475, G476 and N477 are more tolerant in the BA.3. In addition, positions 502–506 in the BA.3 variant (Fig. 5E) are more tolerant to mutations than the respective sites in the BA.2 (Fig. 5B). The mutational maps for BA.3 and BA.4/BA.5 variants revealed common patterns of energetic changes and pointed to shared binding hotspots (Fig. 5E and F) reflecting similarity of the binding interface residues in these complexes (Fig. 5G and H). However, we also found some noticeable differences in the mutational scanning of BA.4/BA.5 RBD complex. Notably, the R403, N417, V445, A475, G476, N477, V486 and N487 sites become much "softer" and more tolerant to substitutions as mutations in these positions induce very minor changes and could be moderately stabilizing in the BA.4/BA.5 complex (Fig. 5F). Overall, the observed differences in the mutational scanning map of the BA.4/BA.5 RBD complex showed a broadly distributed weakening of binding interactions across various segments of the binding interface. At the same time, highly destabilizing mutation-induced changes were observed in positions Y453, L455, F456, Y489, T500, Y501 and H505 (Fig. 5F).

In agreement with deep mutational scanning experiments[122,123] we predicted that the F486V mutation would only slightly reduce the affinity of the BA.4/BA.5 RBD with ACE2. Indeed, according to the mutational scanning analysis, modifications in the V486 position of BA.4/BA.5 RBD induce small dynamic and energetic changes, (Fig. 5F). At the same time, the reversal R493Q can reestablish a hydrogen bond interaction with ACE2 K31 residue in the BA.4/BA.5 complex that was lost due to the charge repulsion between R493 and K31. As a result, mutational changes in Q493 position of the BA.4/BA.5 RBD-ACE2 complex are moderately destabilizing (Fig. 5F). The experimental data showed that the reversal R493Q mutation combined with F486V/L452R changes in BA.4/BA.5 may enhance the immune escape while maintaining the binding affinity comparable to the Omicron BA.1 variant.[52–54] According to our analysis, L452R does not belong to the binding interface in the BA.4/BA.5 complex and therefore may cause relatively small effect on the ACE2 binding. Combined with the observed small compensatory

energetic changes induced by F486V and R493Q mutations, it appeared that a combination of L452R, F486V and R493Q mutations may be exploited by the Omicron BA.4/5 variant to promote the immune escape potential without incurring appreciable reduction of ACE2 binding.

In summary, we found that mutational scanning maps of binding interactions for BA.2 and BA.3 variants were still quite similar, which is consistent with the structural studies and binding affinity measurements. At the same time, more significant differences were observed for BA.4/BA.5 RBD where functional sites become more tolerant to substitutions, reflecting a more dynamic and conformationally adaptable RBD structure in this Omicron subvariant.

Perturbation response scanning reveals variant-specific modulation of allosteric communication routes in the RBD-ACE2 complexes

Using the PRS method, we probed the allosteric effector and sensor potential of the RBD residues in RBD-ACE2 complexes. In this model, the local maxima along the effector profile can serve as indicators of allosteric hotspots that can influence dynamic changes in other residues and may control signal transmission in the system. The effector peaks corresponding to the RBD sites with a high allosteric potential (residues 338–340, 348–353, 400–406, 420–422, 432–436, 450–456, 505–512) are conserved across all RBD-ACE2 complexes (Fig. 6A and B) The highest peaks are aligned with the hydrophobic RBD core residues 399–402 and a β7 core RBD segment (residues 506–512) that connects N501Y and Y505H interfacial positions with the central RBD core. The major allosteric effector clusters were found in the RBD core (residue 348–353) and functionally important segment 450–456 connecting the central core with the binding interface (Fig. 6A and B). The effector cluster peaks were more pronounced for BA.2 and BA.3 RBDs indicating that the allosteric potential of these RBD residues is enhanced in these variants. Together, these observations suggest that BA.2 and BA.3 RBD may feature a robust network of stable allosteric centers that could mediate an ensemble of well-defined signaling paths from the RBD core to the interface regions connecting to the hotspots near R498/Y501 mutational sites. A more dynamic nature of the BA.1 and especially BA.4/BA.5 complexes yielded the effector profile with a more "diffuse" distribution of weak allosteric mediators (Fig. 6A and B). By mapping positions of the BA.2 mutational sites on the PRS profiles (Fig. 6A), we noticed that the effector centers are typically not targeted by Omicron mutations, as these hotspots usually correspond to structural stable positions essential for allosteric communication and signal transmission between the RBD and ACE2 proteins. However, a stronger allosteric potential was found for Q493R, Q498R, and especially N501Y and Y505H residues in the BA.2 and BA.3 variants (Fig. 6). These findings suggested that BA.2 mutations can induce the increased stabilization of the RBD and also amplify the allosteric potential of the key binding hotspots, thereby increasing the efficiency of long-range communications between the RBD and ACE2 proteins.

The sensor profile and respective distribution peaks highlighted residues that have a strong propensity to sense signals and produce allosteric response through altered dynamics. The analysis revealed variant-specific modulation of the PRS sensor

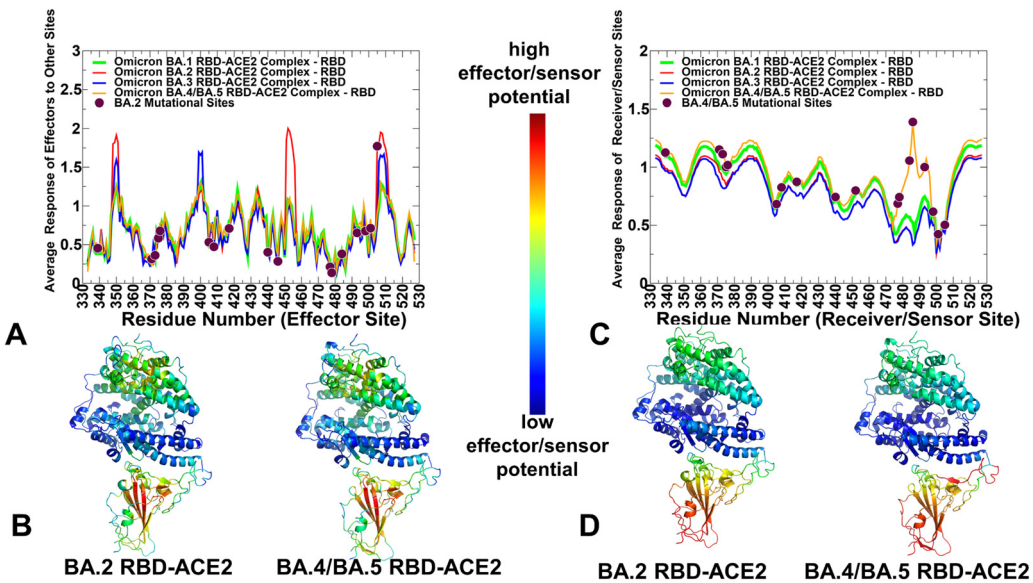

Fig. 6 The PRS analysis of the SARS-CoV-2 Omicron RBD-ACE2 (A) The PRS effector profiles for the BA.1 RBD (in green lines), BA.2 RBD (in red lines), BA.3 RBD (in blue lines) and BA.4/BA.5 RBD (in orange lines). The positions of BA.2 RBD mutational sites (G339D, S371F, S373P, S375F, T376A, D405N, R408S, K417N, N440K, S477N, T478K, E484A, Q493R, Q498R, N501Y, Y505H) are indicated by maroon-colored filled circles. (B) Structural maps of the PRS effector profiles are shown for the BA.2 RBD and BA.4/BA.5 RBD. The color gradient from blue to red indicates the increasing effector propensities. (C) The PRS sensor/receiver profiles for the BA.1 RBD (in green lines), BA.2 RBD (in red lines), BA.3 RBD (in blue lines) and BA.4/BA.5 RBD (in orange lines). The positions of BA.4/BA.5 RBD mutational sites (G339D, S371F, S373P, S375F, T376A, D405N, R408S,K417N, N440K, L452R, S477N, T478K, E484A, F486V, Q493, Q498R, N501Y, Y505H) are indicated by maroon-colored filled circles. (D) Structural maps of the PRS sensor profiles are shown for the BA.2 RBD and BA.4/BA.5 RBD.

profiles, in which BA.2 and BA.3 RBDs have similar distributions and small peaks associated with the flexible RBD regions that may transmit the allosteric signals from the regulatory sites (Fig. 6C and D). The PRS results suggested that for BA.2 and BA.3 complexes major allosteric communication routes would likely proceed through the central binding hub formed by R498, Y501 and H505 residues.

A different scenario may occur for the BA.4/BA.5 complex in which a strong peak of the PRS sensor profile was associated with the flexible RBM region harboring Omicron mutational sites S477N, T478K, E484A, F486V, and Q493 (Fig. 6C and D). These findings suggested that allosteric communications between the RBD and ACE2 in BA.4/BA.5 variant may form a broad ensemble passing through flexible Omicron sites E484A and F486V. Given that F486V can moderately reduce the binding affinity of BA.4/BA.5 RBD with ACE2, this thermodynamic effect may be counterbalanced by the kinetic preferences, providing an explanation to the increased transmission of BA.4/BA.5 variants. Moreover, by increasing the dynamics of the RBM region, the E484A/F486V mutations may promote increased flexibility and induce conformational changes that would limit binding of neutralizing antibodies. To summarize, the PRS results also indicated that Omicron mutational sites can be dynamically coupled through both local and long-range interactions, forming an adaptive allosteric network that controls balance between conformational plasticity, protein stability, and functional adaptability.

Mutational profiling of allosteric communications reveals role of omicron mutations as mediators of allosteric signaling and epistatic couplings

We complemented the PRS results with the network-based mutational profiling of allosteric residue propensities[72,77,78] that are computed using topological network parameters SPC and ASPL (see Materials and Methods) and can characterize the effect of mutations on long-range interactions and global network of allosteric communications in the RBD-ACE2 complexes. Through ensemble-based averaging over mutation-induced changes in these network metrics, the proposed model can identify positions in which mutations on average cause network changes. Allosteric hotspots are identified as residues in which mutations incur significant perturbations of the global residue interaction network that disrupt the network connectivity and cause a significant impairment of global network communications and compromise signaling. By performing *in silico* version of "deep" mutational scans to measure the allosteric effects in the RBD-ACE2 complexes, we examine the variant-induced network changes in the background of the original Wu-Hu-1 strain. Using the network-based mutational profiling approach, we can characterize whether Omicron mutations cause synergistic changes in allosteric communications that may emulate potential epistatic couplings in the effects of mutations at other sites. By systematically introducing mutational changes in the RBD, we computed the ensemble-averaged mutation-induced changes in the SPC network parameter (Fig. 7). The distributions

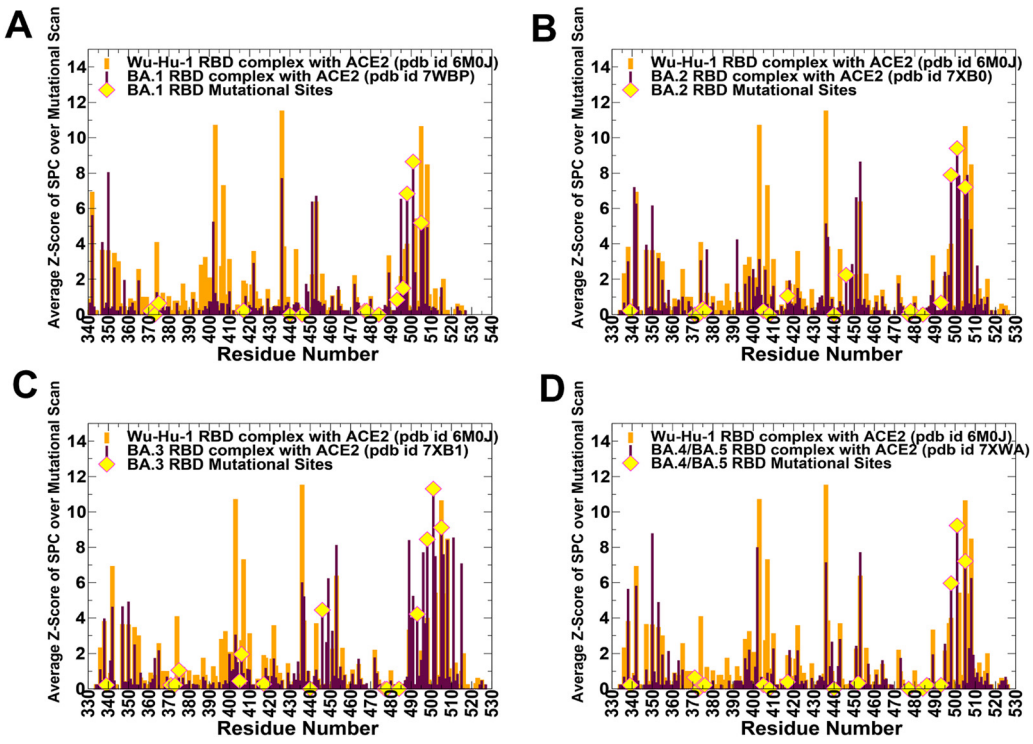

Fig. 7 The dynamic network-based analysis of the Omicron RBD subvariant complexes with ACE2 in the background of the original Wu-Hu-1 strain. The Z-score of SPC centrality for RBD residues averaged over mutational scan for the BA.1 RBD-ACE2 complex (A), BA.2 RBD-ACE2 complex (B), BA.3 RBD-ACE2 complex (C) and BA.4/BA.5 RBD-ACE2 complex (D). The distributions for Omicron RBDs are shown in maroon bars and the distribution for the Wu-Hu-1 RBD is shown in orange bars. The positions of the Omicron mutations are highlighted on the distribution profiles in yellow-colored filled circles.

revealed several clusters of residues important for mediating allosteric communications, including the RBD core segments (340–355, 400–410, 430–450) and binding interface residues 495–505 (Fig. 7).

While in the background Wu-Hu-1 variant the distribution is dominated by the RBD core clusters (residues 400–410 and 430–450), Omicron BA.2 (Fig. 7B) and BA.3 variants (Fig. 7C) can induce changes in the relative contribution of allosteric centers towards the binding interface region anchored by R498, Y501 and H505 positions. Moreover, the profiles for BA.2 and BA.3 variants displayed a dense cluster of allosteric centers (residues 495–510) that links the RBD core residues with the binding interface hotspots R498, Y501 and H505. In both BA.2 and BA.3 profiles, we observed a synergistic increase in allosteric propensities of Omicron mutations R498, Y501 and H505 as compared to the background distribution. This may exemplify the enhanced density of allosteric communication routes in BA.2 passing through the binding hotspots that may act cooperatively and exert potential epistatic effects. In contrast, the distribution for the BA.4/BA.5 complex was more similar to the Wu-Hu-1 profile (Fig. 7D). Nonetheless, the peaks associated with R498 and Y501 residues also emerged synchronously and were appreciably larger than the Z-scores for Q498 and N501 in the original strain. In this context, the mutation-induced changes in the network distributions for the Omicron variants are similar to the experimentally determined profile of the epistatic shifts dominated by N501Y and Q498R and less significant shifts experienced by residues 446–449 and residues 505, 506.[124,125]

Perturbation-based profiling of allosteric residue propensities using mutational scanning of the ASPL changes provided more information about potential allosteric hotspots by mapping a space of network-altering RBD residues (Fig. 8). In this model, we characterize residues where mutations on average induce a significant increase in the ASPL metric and therefore have a dramatic effect on the efficiency of long-range communications in the allosteric interaction network. This analysis enables identification of allosteric control points that could determine the efficient and robust long-range communications in the complexes. The distributions of the average Z-score of ASPL over mutations are characterized by a group of conserved peaks that are shared across all complexes. The commonly shared allosterically important positions include F338, V341, F342, F347, V350, F377, F392, 400–403, W436, Y451, L452, Y495, Y505H, and Y508 (Fig. 8). A significant fraction of these allosteric hotspots are strategically located in the RBD core and mediate network of communications between the RBD residues. Another important revelation was an appreciable correspondence between the PRS effector centers (residues 348–353, 400–406, 420–422, 432–436, 505–512) and the predicted allosteric centers.

The distributions revealed significant differences that can be exemplified by comparison of BA.1 (Fig. 8A) and BA.2 variants (Fig. 8B) in the background of the original strain.

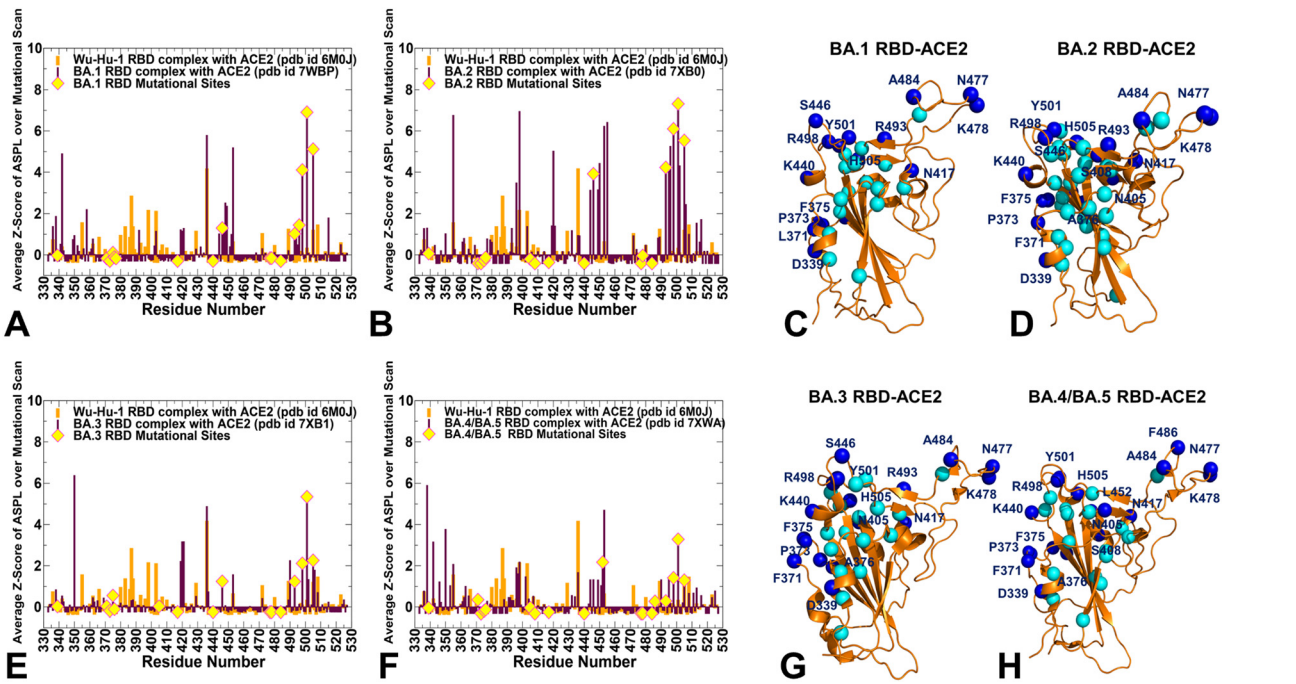

Fig. 8 The dynamic network-based analysis of the Omicron RBD subvariant complexes with ACE2 in the background of the original Wu-Hu-1 strain. The Z-score of ASPL for RBD residues averaged over mutational scan for the BA.1 RBD-ACE2 complex (A), BA.2 RBD-ACE2 complex (B), BA.3 RBD-ACE2 complex (E) and BA.4/BA.5 RBD-ACE2 complex (F). The distributions for Omicron RBDs are shown in maroon bars and the distribution for the Wu-Hu-1 RBD is shown in orange bars. The positions of the Omicron mutations are highlighted on the distribution profiles in yellow-colored filled circles. Structural mapping of the RBD residues with high allosteric potential (in cyan spheres) is shown for the BA.1 RBD-ACE2 complex (C), BA.2 RBD-ACE2 complex (D), BA.3 RBD-ACE2 complex (G) and BA.4/BA.5 RBD-ACE2 complex (H). The Omicron mutational sites are in blue spheres and annotated.

Strikingly, we found that BA.2 variant mutations induced significant redistribution of the Wu-Hu-1 profile, resulting in the emergence of two major clusters of allosteric sites. The major allosteric cluster is fairly broad (residues 495–510) and is anchored by R498, Y501 and H505 BA.2 sites that dominate the distribution (Fig. 8B). Notably, Y501 is aligned with the largest peak in this cluster.

These observations highlighted the collective emergence of these sites as major allosteric mediating centers in the background of the original strain. In network terms, this implies strong synergistic couplings between R498, Y501 and H505 centers to preferentially direct allosteric communications between the RBD and ACE2 molecules. As our analysis is based on systematic mutational scanning of allosteric residue potentials measuring changes in the average short paths, the synergistic emergence of these peaks in BA.2 may be interpreted as a sign of epistatic interactions in which residues 496–505 (including R498 and H505 sites) can acquire the greater allosteric potential in the presence of the N501Y. In addition, we also noticed that a secondary peak of the distribution is located near residues 446–455. These findings agree with the illuminating experimental studies showing that strong high-order epistasis with Q498R/N501Y pair could reduce binding affinity cost of immune escaping mutations.[124,125] According to our results, epistatic couplings between R498, Y501 and H505 can modulate not only the binding affinity to the host receptor ACE2 but also determine allosteric communications and preferential routes of signal transmission in the Omicron complexes.

The distribution of the average Z-score of ASPL over mutations in BA.3 (Fig. 8E) is similar to that of BA.2 (Fig. 8B). However, BA.4/BA.5 mutations induced a distinct modulation profile (Fig. 8F) resulting in a broader distribution of mediating centers. These findings provide further support to our hypothesis that allosteric signaling in the BA.4/BA.5 RBD-ACE2 complex may be propagated *via* a broader ensemble of communication routes. The findings of this analysis also suggested that epistatic couplings between R498, Y501 and H505 can synergistically regulate not only ACE2 binding but also affect allosteric communication and long-range couplings in the Omicron complexes. The experimental data showed that the Q498R mutation alone affected the ACE2 affinity only very moderately[126] but in the background of N501Y, the binding affinity could significantly increase.[124,125] Our results showed that epistatic couplings of R498/Y501 may also promote an efficient long-range communication between RBD and ACE2 which may manifest in the increased transmissibility and allow accumulation of multiple immune escape mutations at other sites and corresponding greater virus adaptability for immune escape.[124,125]

Structural mapping of the distribution peaks for BA.1 (Fig. 8C), BA.2 (Fig. 8D), BA.3 (Fig. 8G) and BA.4/BA.5 (Fig. 8H) showed that most of the Omicron mutational sites are located in the immediate vicinity of major allosteric control points. Hence, Omicron mutations for all studied variants may avoid direct targeting of allosterically sensitive sites to retain the spike activity while leveraging their structural proximity to strategic effector positions in the RBD to modulate communication between distant RBD and ACE2 regions.

Discussion

Although mutations in viruses occur randomly as the virus replicates where most of these mutations have no significant effect on the virus's characteristics, the emergence of Omicron mutations affecting transmissibility and pathogenicity features is often interpreted within a trade-off scenario of SARS-CoV-2 evolution which leads to lowered lethality, yet enhanced transmissibility.[127,128] When it comes to immune escape, viruses may undergo mutations that allow them to evade the immune responses generated by the host. This can happen through various mechanisms, such as changes in the viral spike protein that affect its interaction with antibodies or alterations in other viral proteins involved in immune recognition. This direction of evolution might be partly explained by virus adaptation to enhanced escape from vaccine-induced and natural immunity formed by other SARS-CoV-2 strains.

The results of this study provided molecular rationale and support to a mechanism in which the optimized balance of thermodynamic stability and conformational adaptability enabled Omicron variants to induce the increased immune escape and reduced antigenicity that permits evasion of vaccine-induced immunity, while maintaining strong ACE2 binding affinity. It is important to note that while viruses can evolve to escape immune responses, it does not necessarily mean that every mutation will lead to the increased immune escape. Some mutations may have no effect or even reduce the virus's fitness, limiting their spread and impact. Additionally, the immune system is a complex and adaptable defense mechanism, and even if a virus evolves to escape one aspect of the immune response, other components of the immune system may still provide protection.

Our results provided support to the mechanism in which binding affinity hotspots N501Y and Q498R have a coordinated effect on the spike stability, binding, and allostery, allowing new Omicron subvariants to balance virus fitness in the presence of immune-escape mutations. Hence, Omicron variants may have developed mechanisms to evade or reduce the effectiveness of immune responses while still maintaining high ACE2 affinity and RBD stability required for functionality and infectivity. These findings highlight the complexity of viral evolution and the importance of understanding the interplay between viral genetic changes and protein function in response to immune pressure.

Conclusions

In this study, we systematically examined conformational dynamics, stability and binding of the Omicron RBD complexes with ACE2 using microsecond atomistic MD simulations, *in silico* mutational scanning, PRS analysis and network-based mutational profiling of allosteric communications. Consistent

with the experimental data, our results showed that BA.2 mutations may induce the increased stabilization of the RBD in the complex with ACE2 which may be linked with the higher binding affinity than the other variants, while a greater flexibility is an important dynamic signature of the BA.4/BA.5 variants. Through perturbation-response scanning approach and modeling of allosteric interaction networks we examined the thermodynamic and allosteric factors of RBD-ACE2 binding across BA.1, BA.2, BA.3 and BA.4/BA.5 variants. Our findings suggested that BA.2 mutations may not only induce the increased stabilization of the RBD and enhanced binding interface, but also amplify the allosteric potential of the key binding hotspots, thereby increasing the efficiency of preferential routes for long-range communications with ACE2. Network-based mutational profiling approaches probed the effect of the different Omicron variants on allosteric communications, revealing hidden roles of Omicron mutations as evolutionary adaptable modulators of stability, binding and allostery. Through perturbation network scanning of allosteric residue potentials in the Omicron variant complexes, which is performed in the background of the original strain, we identified that the key Omicron binding affinity hotspots N501Y and Q498R could mediate allosteric interactions and epistatic couplings. Through integration of synergistic computational approaches this study provides a systematic analysis of the effects of Omicron mutations on thermodynamics, binding and allosteric signaling in the RBD complexes with the ACE2 receptor.

Author contributions

Conceptualization, G. V. and P. T.; methodology, G. V. and P. T.; software, G. V., S. X., M. A., G. G. and P. T.; validation, G. V.; formal analysis, G. V., M. A., G. G., S. X., and P. T. investigation, G. V. and P. T.; resources, G. V., M. A. and G. G.; data curation, G. V.; writing—original draft preparation, G. V.; writing—review and editing, G. V., M. A. and G. G.; visualization, G. V.; supervision, G. V.; project administration, G. V.; funding acquisition, G. V. All authors have read and agreed to the published version of the manuscript.

Data availability statement

Data is fully contained within the article. The crystal structures were obtained and downloaded from the Protein Data Bank (**https://www.rcsb.org**). All simulations were performed using openMM high-performance toolkit for molecular simulation that was obtained from websites **https://openmm.org/**, **https://simtk.org/projects/openmm** and **https://github.com/openmm/openmm**. All simulations were performed using the all-atom additive CHARMM36 protein force field that can be obtained from **https://mackerell.umaryland.edu/charmm_ff.shtml**. The residue interaction network files were obtained for all structures using the Residue Interaction Network Generator (RING) program RING v2.0.1 freely available at **https://old.protein.bio.unipd.it/ring/**. The rendering of protein structures was done with interactive visualization program UCSF ChimeraX package (**https://www.rbvi.ucsf.edu/chimerax/**) and Pymol (**https://pymol.org/2/**). All the data obtained in this work (including simulation trajectories, topology and parameter files), molecular dynamics analysis tools, and the in-house scripts are freely available at DOI: **https://doi.org/10.5281/zenodo.7889040** (**https://zenodo.org/record/7889041#.ZFKRVs7MI2w**) and in the GitHub sites **https://github.com/smu-tao-group/protein-VAE**; **https://github.com/smu-tao-group/PASSer2.0**.

Conflicts of interest

The authors declare no conflict of interest. The funders had no role in the design of the study; in the collection, analyses, or interpretation of data; in the writing of the manuscript; or in the decision to publish the results.

Acknowledgements

This research was supported by the Kay Family Foundation Grant A20-0032 and National Institutes of Health under Award No. R15GM122013. The authors acknowledge support from Schmid College of Science and Technology at Chapman University for providing computing resources at the Keck Center for Science and Engineering.

References

1 W. Tai, L. He, X. Zhang, J. Pu, D. Voronin, S. Jiang, Y. Zhou and L. Du, Characterization of the receptor-binding domain (RBD) of 2019 novel coronavirus: implication for development of RBD protein as a viral attachment inhibitor and vaccine, *Cell. Mol. Immunol.*, 2020, **17**, 613–620, DOI: **10.1038/s41423-020-0400-4**.

2 Q. Wang, Y. Zhang, L. Wu, S. Niu, C. Song, Z. Zhang, G. Lu, C. Qiao, Y. Hu, K. Y. Yuen, Q. Wang, H. Zhou, J. Yan and J. Qi, Structural and functional basis of SARS-CoV-2 entry by using human ACE2, *Cell*, 2020, **181**, 894–904.e9, DOI: **10.1016/j.cell.2020.03.045**.

3 A. C. Walls, Y. J. Park, M. A. Tortorici, A. Wall, A. T. McGuire and D. Veesler, Structure, Function, and Antigenicity of the SARS-CoV-2 Spike Glycoprotein, *Cell*, 2020, **181**, 281–292.e6, DOI: **10.1016/j.cell.2020.02.058**.

4 D. Wrapp, N. Wang, K. S. Corbett, J. A. Goldsmith, C. L. Hsieh, O. Abiona, B. S. Graham and J. S. McLellan, Cryo-EM structure of the 2019-nCoV spike in the prefusion conformation, *Science*, 2020, **367**, 1260–1263, DOI: **10.1126/science.abb2507**.

5 Y. Cai, J. Zhang, T. Xiao, H. Peng, S. M. Sterling, R. M. Walsh, S. Rawson, S. Rits-Volloch and B. Chen, Distinct conformational states of SARS-CoV-2 spike protein, *Science*, 2020, **369**, 1586–1592, DOI: **10.1126/science.abd4251**.

6 C. L. Hsieh, J. A. Goldsmith, J. M. Schaub, A. M. DiVenere, H. C. Kuo, K. Javanmardi, K. C. Le, D. Wrapp, A. G. Lee,

Y. Liu, C. W. Chou, P. O. Byrne, C. K. Hjorth, N. V. Johnson, J. Ludes-Meyers, A. W. Nguyen, J. Park, N. Wang, D. Amengor, J. J. Lavinder, G. C. Ippolito, J. A. Maynard, I. J. Finkelstein and J. S. McLellan, Structure-based design of prefusion-stabilized SARS-CoV-2 spikes, *Science*, 2020, **369**, 1501–1505, DOI: **10.1126/science.abd0826**.

7 R. Henderson, R. J. Edwards, K. Mansouri, K. Janowska, V. Stalls, S. M. C. Gobeil, M. Kopp, D. Li, R. Parks, A. L. Hsu, M. J. Borgnia, B. F. Haynes and P. Acharya, Controlling the SARS-CoV-2 spike glycoprotein conformation, *Nat. Struct. Mol. Biol.*, 2020, **27**, 925–933, DOI: **10.1038/s41594-020-0479-4**.

8 M. McCallum, A. C. Walls, J. E. Bowen, D. Corti and D. Veesler, Structure-guided covalent stabilization of coronavirus spike glycoprotein trimers in the closed conformation, *Nat. Struct. Mol. Biol.*, 2020, **27**, 942–949, DOI: **10.1038/s41594-020-0483-8**.

9 X. Xiong, K. Qu, K. A. Ciazynska, M. Hosmillo, A. P. Carter, S. Ebrahimi, Z. Ke, S. H. W. Scheres, L. Bergamaschi, G. L. Grice, Y. Zhang, CITIID-NIHR COVID-19 BioResource Collaboration, J. A. Nathan, S. Baker, L. C. James, H. E. Baxendale, I. Goodfellow, R. Doffinger and J. A. G. Briggs, A thermostable, closed SARS-CoV-2 spike protein trimer, *Nat. Struct. Mol. Biol.*, 2020, **27**, 934–941, DOI: **10.1038/s41594-020-0478-5**.

10 S. M. Costello, S. R. Shoemaker, H. T. Hobbs, A. W. Nguyen, C. L. Hsieh, J. A. Maynard, J. S. McLellan, J. E. Pak and S. Marqusee, The SARS-CoV-2 spike reversibly samples an open-trimer conformation exposing novel epitopes, *Nat. Struct. Mol. Biol.*, 2022, **27**, 229–238, DOI: **10.1038/s41594-022-00735-5**.

11 K. D. McCormick, J. L. Jacobs and J. W. Mellors, The emerging plasticity of SARS-CoV-2, *Science*, 2021, **371**, 1306–1308, DOI: **10.1126/science.abg4493**.

12 D. Ghimire, Y. Han and M. Lu, Structural Plasticity and Immune Evasion of SARS-CoV-2 Spike Variants, *Viruses*, 2022, **14**, 1255, DOI: **10.3390/v14061255**.

13 C. Xu, Y. Wang, C. Liu, C. Zhang, W. Han, X. Hong, Y. Wang, Q. Hong, S. Wang, Q. Zhao, Y. Wang, Y. Yang, K. Chen, W. Zheng, L. Kong, F. Wang, Q. Zuo, Z. Huang and Y. Cong, Conformational dynamics of SARS-CoV-2 trimeric spike glycoprotein in complex with receptor ACE2 revealed by cryo-EM, *Sci. Adv.*, 2021, **7**, eabe5575, DOI: **10.1126/sciadv.abe5575**.

14 D. J. Benton, A. G. Wrobel, P. Xu, C. Roustan, S. R. Martin, P. B. Rosenthal, J. J. Skehel and S. J. Gamblin, Receptor binding and priming of the spike protein of SARS-CoV-2 for membrane fusion, *Nature*, 2020, **588**, 327–330, DOI: **10.1038/s41586-020-2772-0**.

15 B. Turoňová, M. Sikora, C. Schürmann, W. J. H. Hagen, S. Welsch, F. E. C. Blanc, S. von Bülow, M. Gecht, K. Bagola, C. Hörner, G. van Zandbergen, J. Landry, N. T. D. de Azevedo, S. Mosalaganti, A. Schwarz, R. Covino, M. D. Mühlebach, G. Hummer, J. Krijnse Locker and M. Beck, In situ structural analysis of SARS-CoV-2 spike reveals flexibility mediated by three hinges, *Science*, 2020, **370**, 203–208, DOI: **10.1126/science.abd5223**.

16 M. Lu, P. D. Uchil, W. Li, D. Zheng, D. S. Terry, J. Gorman, W. Shi, B. Zhang, T. Zhou, S. Ding, R. Gasser, J. Prevost, G. Beaudoin-Bussieres, S. P. Anand, A. Laumaea, J. R. Grover, L. Lihong, D. D. Ho, J. R. Mascola, A. Finzi, P. D. Kwong, S. C. Blanchard and W. Mothes, Real-time conformational dynamics of SARS-CoV-2 spikes on virus particles, *Cell Host Microbe*, 2020, **28**, 880–891.e8, DOI: **10.1016/j.chom.2020.11.001**.

17 Z. Yang, Y. Han, S. Ding, W. Shi, T. Zhou, A. Finzi, P. D. Kwong, W. Mothes and M. Lu, SARS-CoV-2 Variants Increase Kinetic Stability of Open Spike Conformations as an Evolutionary Strategy, *mBio*, 2022, **13**, e0322721, DOI: **10.1128/mbio.03227-21**.

18 M. A. Díaz-Salinas, Q. Li, M. Ejemel, L. Yurkovetskiy, J. Luban, K. Shen, Y. Wang and J. B. Munro, Conformational dynamics and allosteric modulation of the SARS-CoV-2 spike, *eLife*, 2022, **11**, e75433, DOI: **10.7554/eLife.75433**.

19 P. Han, L. Li, S. Liu, Q. Wang, D. Zhang, Z. Xu, X. Li, Q. Peng, C. Su, B. Huang, D. Li, R. Zhang, M. Tian, L. Fu, Y. Gao, X. Zhao, K. Liu, J. Qi, G. F. Gao and P. Wang, Receptor binding and complex structures of human ACE2 to spike RBD from omicron and delta SARS-CoV-2, *Cell*, 2022, **185**, 630–640.e10, DOI: **10.1016/j.cell.2022.01.001**.

20 J. W. Saville, D. Mannar, X. Zhu, S. S. Srivastava, A. M. Berezuk, J. P. Demers, S. Zhou, K. S. Tuttle, I. Sekirov, A. Kim, W. Li, D. S. Dimitrov and S. Subramaniam, Structural and biochemical rationale for enhanced spike protein fitness in delta and kappa SARS-CoV-2 variants, *Nat. Commun.*, 2022, **13**, 742, DOI: **10.1038/s41467-022-28324-6**.

21 Y. Wang, C. Liu, C. Zhang, Y. Wang, Q. Hong, S. Xu, Z. Li, Y. Yang, Z. Huang and Y. Cong, Structural basis for SARS-CoV-2 Delta variant recognition of ACE2 receptor and broadly neutralizing antibodies, *Nat. Commun.*, 2022, **13**, 871, DOI: **10.1038/s41467-022-28528-w**.

22 J. Zhang, T. Xiao, Y. Cai, C. L. Lavine, H. Peng, H. Zhu, K. Anand, P. Tong, A. Gautam, M. L. Mayer, R. M. Walsh, S. Rits-Volloch, D. R. Wesemann, W. Yang, M. S. Seaman, J. Lu and B. Chen, Membrane fusion and immune evasion by the spike protein of SARS-CoV-2 Delta variant, *Science*, 2021, **374**, 1353–1360, DOI: **10.1126/science.abl9463**.

23 D. Mannar, J. W. Saville, X. Zhu, S. S. Srivastava, A. M. Berezuk, K. S. Tuttle, A. C. Marquez, I. Sekirov and S. Subramaniam, SARS-CoV-2 Omicron variant: Antibody evasion and cryo-EM structure of spike protein-ACE2 complex, *Science*, 2022, **375**, 760–764, DOI: **10.1126/science.abn7760**.

24 Q. Hong, W. Han, J. Li, S. Xu, Y. Wang, C. Xu, Z. Li, Y. Wang, C. Zhang, Z. Huang and Y. Cong, Molecular basis of receptor binding and antibody neutralization of Omicron, *Nature*, 2022, **604**, 546–552, DOI: **10.1038/s41586-022-04581-9**.

25 M. McCallum, N. Czudnochowski, L. E. Rosen, S. K. Zepeda, J. E. Bowen, A. C. Walls, K. Hauser, A. Joshi, C. Stewart, J. R. Dillen, A. E. Powell, T. I. Croll, J. Nix,

H. W. Virgin, D. Corti, G. Snell and D. Veesler, Structural basis of SARS-CoV-2 Omicron immune evasion and receptor engagement, *Science*, 2022, **375**, 864–868, DOI: **10.1126/science.abn8652**.

26 W. Yin, Y. Xu, P. Xu, X. Cao, C. Wu, C. Gu, X. He, X. Wang, S. Huang, Q. Yuan, K. Wu, W. Hu, Z. Huang, J. Liu, Z. Wang, F. Jia, K. Xia, P. Liu, X. Wang, B. Song, J. Zheng, H. Jiang, X. Cheng, Y. Jiang, S. J. Deng and H. E. Xu, Structures of the Omicron Spike trimer with ACE2 and an anti-Omicron antibody, *Science*, 2022, **375**, 1048–1053, DOI: **10.1126/science.abn8863**.

27 S. M.-C. Gobeil, R. Henderson, V. Stalls, K. Janowska, X. Huang, A. May, M. Speakman, E. Beaudoin, K. Manne, D. Li, R. Parks, M. Barr, M. Deyton, M. Martin, K. Mansouri, R. J. Edwards, A. Eaton, D. C. Montefiori, G. D. Sempowski, K. O. Saunders, K. Wiehe, W. Williams, B. Korber, B. F. Haynes and P. Acharya, Structural Diversity of the SARS-CoV-2 Omicron Spike, *Mol. Cell*, 2022, **82**, 2050–2068.e6, DOI: **10.1016/j.molcel.2022.03.028**.

28 Z. Cui, P. Liu, N. Wang, L. Wang, K. Fan, Q. Zhu, K. Wang, R. Chen, R. Feng, Z. Jia, M. Yang, G. Xu, B. Zhu, W. Fu, T. Chu, L. Feng, Y. Wang, X. Pei, P. Yang, X. S. Xie, L. Cao, Y. Cao and X. Wang, Structural and functional characterizations of infectivity and immune evasion of SARS-CoV-2 Omicron, *Cell*, 2022, **185**, 860–871.e13, DOI: **10.1016/j.cell.2022.01.019**.

29 T. Zhou, L. Wang, J. Misasi, A. Pegu, Y. Zhang, D. R. Harris, A. S. Olia, C. A. Talana, E. S. Yang, M. Chen, M. Choe, W. Shi, I. T. Teng, A. Creanga, C. Jenkins, K. Leung, T. Liu, E. D. Stancofski, T. Stephens, B. Zhang, Y. Tsybovsky, B. S. Graham, J. R. Mascola, N. J. Sullivan and P. D. Kwong, Structural basis for potent antibody neutralization of SARS-CoV-2 variants including B.1.1.529, *Science*, 2022, **376**, eabn8897, DOI: **10.1126/science.abn8897**.

30 H. Guo, Y. Gao, T. Li, T. Li, Y. Lu, L. Zheng, Y. Liu, T. Yang, F. Luo, S. Song, W. Wang, X. Yang, H. C. Nguyen, H. Zhang, A. Huang, A. Jin, H. Yang, Z. Rao and X. Ji, Structures of Omicron Spike Complexes and Implications for Neutralizing Antibody Development, *Cell Rep.*, 2022, **39**, 110770, DOI: **10.1016/j.celrep.2022.110770**.

31 V. Stalls, J. Lindenberger, S. M.-C. Gobeil, R. Henderson, R. Parks, M. Barr, M. Deyton, M. Martin, K. Janowska, X. Huang, A. May, M. Speakman, E. Beaudoin, B. Kraft, X. Lu, R. J. Edwards, A. Eaton, D. C. Montefiori, W. B. Williams, K. O. Saunders, K. Wiehe, B. F. Haynes and P. Acharya, Cryo-EM Structures of SARS-CoV-2 Omicron BA.2 Spike, *Cell Rep.*, 2022, **39**, 111009, DOI: **10.1016/j.celrep.2022.111009**.

32 S. Lin, Z. Chen, X. Zhang, A. Wen, X. Yuan, C. Yu, J. Yang, B. He, Y. Cao and G. Lu, Characterization of SARS-CoV-2 Omicron Spike RBD Reveals Significantly Decreased Stability, Severe Evasion of Neutralizing-Antibody Recognition but Unaffected Engagement by Decoy ACE2 Modified for Enhanced RBD Binding, *Signal Transduction Targeted Ther.*, 2022, **7**, 6, DOI: **10.1038/s41392-022-00914-2**.

33 Z. Zhao, J. Zhou, M. Tian, M. Huang, S. Liu, Y. Xie, P. Han, C. Bai, P. Han, A. Zheng, L. Fu, Y. Gao, Q. Peng, Y. Li, Y. Chai, Z. Zhang, X. Zhao, H. Song, J. Qi, Q. Wang, P. Wang and G. F. Gao, Omicron SARS-CoV-2 Mutations Stabilize Spike up-RBD Conformation and Lead to a Non-RBM-Binding Monoclonal Antibody Escape, *Nat. Commun.*, 2022, **13**, 4958, DOI: **10.1038/s41467-022-32665-7**.

34 G. Cerutti, Y. Guo, L. Liu, L. Liu, Z. Zhang, Y. Luo, Y. Huang, H. H. Wang, D. D. Ho, Z. Sheng and L. Shapiro, Cryo-EM Structure of the SARS-CoV-2 Omicron Spike, *Cell Rep.*, 2022, **38**, 110428, DOI: **10.1016/j.celrep.2022.110428**.

35 G. Ye, B. Liu and F. Li, Cryo-EM Structure of a SARS-CoV-2 Omicron Spike Protein Ectodomain, *Nat. Commun.*, 2022, **13**, 1214, DOI: **10.1038/s41467-022-28882-9**.

36 W. Dejnirattisai, J. Huo, D. Zhou, J. Zahradník, P. Supasa, C. Liu, H. M. E. Duyvesteyn, H. M. Ginn, A. J. Mentzer, A. Tuekprakhon, R. Nutalai, B. Wang, A. Dijokaite, S. Khan, O. Avinoam, M. Bahar, D. Skelly, S. Adele, S. A. Johnson, A. Amini, T. G. Ritter, C. Mason, C. Dold, D. Pan, S. Assadi, A. Bellass, N. Omo-Dare, D. Koeckerling, A. Flaxman, D. Jenkin, P. K. Aley, M. Voysey, S. A. Costa Clemens, F. G. Naveca, V. Nascimento, F. Nascimento, C. Fernandes da Costa, P. C. Resende, A. Pauvolid-Correa, M. M. Siqueira, V. Baillie, N. Serafin, G. Kwatra, K. Da Silva, S. A. Madhi, M. C. Nunes, T. Malik, P. J. M. Openshaw, J. K. Baillie, M. G. Semple, A. R. Townsend, K. A. Huang, T. K. Tan, M. W. Carroll, P. Klenerman, E. Barnes, S. J. Dunachie, B. Constantinides, H. Webster, D. Crook, A. J. Pollard, T. Lambe, N. G. Paterson, M. A. Williams, D. R. Hall, E. E. Fry, J. Mongkolsapaya, J. Ren, G. Schreiber, D. I. Stuart and G. R. Screaton, SARS-CoV-2 Omicron-B.1.1.529 leads to widespread escape from neutralizing antibody responses, *Cell*, 2022, **185**, 467–484.e415, DOI: **10.1016/j.cell.2021.12.046**.

37 E. Cameroni, J. E. Bowen, L. E. Rosen, C. Saliba, S. K. Zepeda, K. Culap, D. Pinto, L. A. VanBlargan, A. De Marco, J. di Iulio, F. Zatta, H. Kaiser, J. Noack, N. Farhat, N. Czudnochowski, C. Havenar-Daughton, K. R. Sprouse, J. R. Dillen, A. E. Powell, A. Chen, C. Maher, L. Yin, D. Sun, L. Soriaga, J. Bassi, C. Silacci-Fregni, C. Gustafsson, N. M. Franko, J. Logue, N. T. Iqbal, I. Mazzitelli, J. Geffner, R. Grifantini, H. Chu, A. Gori, A. Riva, O. Giannini, A. Ceschi, P. Ferrari, P. E. Cippà, A. Franzetti-Pellanda, C. Garzoni, P. J. Halfmann, Y. Kawaoka, C. Hebner, L. A. Purcell, L. Piccoli, M. S. Pizzuto, A. C. Walls, M. S. Diamond, A. Telenti, H. W. Virgin, A. Lanzavecchia, G. Snell, D. Veesler and D. Corti, Broadly neutralizing antibodies overcome SARS-CoV-2 Omicron antigenic shift, *Nature*, 2022, **602**, 664–670, DOI: **10.1038/s41586-021-04386-2**.

38 M. I. Barton, S. A. MacGowan, M. A. Kutuzov, O. Dushek, G. J. Barton and P. A. van der Merwe, Effects of common mutations in the SARS-CoV-2 Spike RBD and its ligand, the human ACE2 receptor on binding affinity and kinetics, *eLife*, 2021, **10**, e70658, DOI: **10.7554/eLife.70658**.

39 Y. Cao, J. Wang, F. Jian, T. Xiao, W. Song, A. Yisimayi, W. Huang, Q. Li, P. Wang, R. An, J. Wang, Y. Wang, X. Niu, S. Yang, H. Liang, H. Sun, T. Li, Y. Yu, Q. Cui, S. Liu, X. Yang, S. Du, Z. Zhang, X. Hao, F. Shao, R. Jin, X. Wang, J. Xiao, Y. Wang and X. S. Xie, Omicron escapes the majority of existing SARS-CoV-2 neutralizing antibodies, *Nature*, 2022, **602**, 657–663, DOI: **10.1038/s41586-021-04385-3**.

40 L. Liu, S. Iketani, Y. Guo, J. F. Chan, M. Wang, L. Liu, Y. Luo, H. Chu, Y. Huang, M. S. Nair, J. Yu, K. K. Chik, T. T. Yuen, C. Yoon, K. K. To, H. Chen, M. T. Yin, M. E. Sobieszczyk, Y. Huang, H. H. Wang, Z. Sheng, K. Y. Yuen and D. D. Ho, Striking antibody evasion manifested by the Omicron variant of SARS-CoV-2, *Nature*, 2022, **602**, 676–681, DOI: **10.1038/s41586-021-04388-0**.

41 J. Zhang, Y. Cai, C. L. Lavine, H. Peng, H. Zhu, K. Anand, P. Tong, A. Gautam, M. L. Mayer, S. Rits-Volloch, S. Wang, P. Sliz, D. R. Wesemann, W. Yang, M. S. Seaman, J. Lu, T. Xiao and B. Chen, Structural and functional impact by SARS-CoV-2 Omicron spike mutations, *Cell Rep.*, 2022, **39**, 110729, DOI: **10.1016/j.celrep.2022.110729**.

42 R. Zhu, D. Canena, M. Sikora, M. Klausberger, H. Seferovic, A. R. Mehdipour, L. Hain, E. Laurent, V. Monteil, G. Wirnsberger, R. Wieneke, R. Tampé, N. F. Kienzl, L. Mach, A. Mirazimi, Y. J. Oh, J. M. Penninger, G. Hummer and P. Hinterdorfer, Force-Tuned Avidity of Spike Variant-ACE2 Interactions Viewed on the Single-Molecule Level, *Nat. Commun.*, 2022, **13**, 7926, DOI: **10.1038/s41467-022-35641-3**.

43 M. S. Bauer, S. Gruber, A. Hausch, P. S. F. C. Gomes, L. F. Milles, T. Nicolaus, L. C. Schendel, P. L. Navajas, E. Procko, D. Lietha, M. C. R. Melo, R. C. Bernardi, H. E. Gaub and J. Lipfert, A tethered ligand assay to probe SARS-CoV-2:ACE2 interactions, *Proc. Natl. Acad. Sci. U. S. A.*, 2022, **119**, e2114397119, DOI: **10.1073/pnas.2114397119** A tethered ligand assay to probe SARS-CoV-2:ACE2 interactions. Proc. Natl. Acad. Sci. U.S.A. 2022, 119, e2114397119. doi: 10.1073/pnas.2114397119.

44 W. Hu, Y. Zhang, P. Fei, T. Zhang, D. Yao, Y. Gao, J. Liu, H. Chen, Q. Lu, T. Mudianto, X. Zhang, C. Xiao, Y. Ye, Q. Sun, J. Zhang, Q. Xie, P. H. Wang, J. Wang, Z. Li, J. Lou and W. Chen, Mechanical activation of spike fosters SARS-CoV-2 viral infection, *Cell Res.*, 2021, **31**, 1047–1060, DOI: **10.1038/s41422-021-00558-x**.

45 L. Li, H. Liao, Y. Meng, W. Li, P. Han, K. Liu, Q. Wang, D. Li, Y. Zhang, L. Wang, Z. Fan, Y. Zhang, Q. Wang, X. Zhao, Y. Sun, N. Huang, J. Qi and G. F. Gao, Structural basis of human ACE2 higher binding affinity to currently circulating Omicron SARS-CoV-2 sub-variants BA.2 and BA.1.1, *Cell*, 2022, **185**, 2952–2960.e10, DOI: **10.1016/j.cell.2022.06.023**.

46 Y. Xu, C. Wu, X. Cao, C. Gu, H. Liu, M. Jiang, X. Wang, Q. Yuan, K. Wu, J. Liu, D. Wang, X. He, X. Wang, S. J. Deng, H. E. Xu and W. Yin, Structural and biochemical mechanism for increased infectivity and immune evasion of Omicron BA.2 variant compared to BA.1 and their possible mouse origins, *Cell Res.*, 2022, **32**, 609–620, DOI: **10.1038/s41422-022-00672-4**.

47 A. Tuekprakhon, R. Nutalai, A. Dijokaite-Guraliuc, D. Zhou, H. M. Ginn, M. Selvaraj, C. Liu, A. J. Mentzer, P. Supasa, H. M. E. Duyvesteyn, R. Das, D. Skelly, T. G. Ritter, A. Amini, S. Bibi, S. Adele, S. A. Johnson, B. Constantinides, H. Webster, N. Temperton, P. Klenerman, E. Barnes, S. J. Dunachie, D. Crook, A. J. Pollard, T. Lambe, P. Goulder, N. G. Paterson, M. A. Williams, D. R. Hall, OPTIC Consortium; ISARIC4C Consortium, E. E. Fry, J. Huo, J. Mongkolsapaya, J. Ren, D. I. Stuart and G. R. Screaton, Antibody escape of SARS-CoV-2 Omicron BA.4 and BA.5 from vaccine and BA.1 serum, *Cell*, 2022, **185**, 2422–2433.e13, DOI: **10.1016/j.cell.2022.06.005**.

48 Y. Cao, A. Yisimayi, F. Jian, W. Song, T. Xiao, L. Wang, S. Du, J. Wang, Q. Li, X. Chen, Y. Yu, P. Wang, Z. Zhang, P. Liu, R. An, X. Hao, Y. Wang, J. Wang, R. Feng, H. Sun, L. Zhao, W. Zhang, D. Zhao, J. Zheng, L. Yu, C. Li, N. Zhang, R. Wang, X. Niu, S. Yang, X. Song, Y. Chai, Y. Hu, Y. Shi, L. Zheng, Z. Li, Q. Gu, F. Shao, W. Huang, R. Jin, Z. Shen, Y. Wang, X. Wang, J. Xiao and X. S. Xie, BA.2.12.1, BA.4 and BA.5 escape antibodies elicited by Omicron infection, *Nature*, 2022, **608**, 593–602, DOI: **10.1038/s41586-022-04980-y**.

49 J. E. Bowen, A. Addetia, H. V. Dang, C. Stewart, J. T. Brown, W. K. Sharkey, K. R. Sprouse, A. C. Walls, I. G. Mazzitelli, J. K. Logue, N. M. Franko, N. Czudnochowski, A. E. Powell, E. Dellota, K. Ahmed, A. S. Ansari, E. Cameroni, A. Gori, A. Bandera, C. M. Posavad, J. M. Dan, Z. Zhang, D. Weiskopf, A. Sette, S. Crotty, N. T. Iqbal, D. Corti, J. Geffner, G. Snell, R. Grifantini, H. Y. Chu and D. Veesler, Omicron spike function and neutralizing activity elicited by a comprehensive panel of vaccines, *Science*, 2022, **377**, 890–894, DOI: **10.1126/science.abq0203**.

50 D. Ni, P. Turelli, B. Beckert, S. Nazarov, E. Uchikawa, A. Myasnikov, F. Pojer, D. Trono, H. Stahlberg and K. Lau, Cryo-EM Structures and Binding of Mouse and Human ACE2 to SARS-CoV-2 Variants of Concern Indicate That Mutations Enabling Immune Escape Could Expand Host Range, *PLoS Pathog.*, 2023, **19**, e1011206, DOI: **10.1371/journal.ppat.1011206**.

51 I. Kimura, D. Yamasoba, T. Tamura, N. Nao, T. Suzuki, Y. Oda, S. Mitoma, J. Ito, H. Nasser, J. Zahradnik, K. Uriu, S. Fujita, Y. Kosugi, L. Wang, M. Tsuda, M. Kishimoto, H. Ito, R. Suzuki, R. Shimizu, M. M. Begum, K. Yoshimatsu, K. T. Kimura, J. Sasaki, K. Sasaki-Tabata, Y. Yamamoto, T. Nagamoto, J. Kanamune, K. Kobiyama, H. Asakura, M. Nagashima, K. Sadamasu, K. Yoshimura, K. Shirakawa, A. Takaori-Kondo, J. Kuramochi, G. Schreiber, K. J. Ishii, T. Hashiguchi, T. Ikeda, A. Saito, T. Fukuhara, S. Tanaka, K. Matsuno and K. Sato, Virological Characteristics of the SARS-CoV-2 Omicron BA.2 Subvariants, Including BA.4 and BA.5, *Cell*, 2022, **185**, 3992–4007.e16, DOI: **10.1016/j.cell.2022.09.018**.

52 J. Huo, A. Dijokaite-Guraliuc, C. Liu, D. Zhou, H. M. Ginn, R. Das, P. Supasa, M. Selvaraj, R. Nutalai, A. Tuekprakhon,

H. M. E. Duyvesteyn, A. J. Mentzer, D. Skelly, T. G. Ritter, A. Amini, S. Bibi, S. Adele, S. A. Johnson, N. G. Paterson, M. A. Williams, D. R. Hall, M. Plowright, T. A. H. Newman, H. Hornsby, T. I. de Silva, N. Temperton, P. Klenerman, E. Barnes, S. J. Dunachie, A. J. Pollard, T. Lambe, P. Goulder, E. E. Fry, J. Mongkolsapaya, J. Ren, D. I. Stuart and G. R. Screaton, A Delicate Balance between Antibody Evasion and ACE2 Affinity for Omicron BA.2.75, *Cell Rep.*, 2023, **42**, 111903, DOI: **10.1016/j.celrep.2022.111903**.

53 Y.-J. Park, D. Pinto, A. C. Walls, Z. Liu, A. De Marco, F. Benigni, F. Zatta, C. Silacci-Fregni, J. Bassi, K. R. Sprouse, A. Addetia, J. E. Bowen, C. Stewart, M. Giurdanella, C. Saliba, B. Guarino, M. A. Schmid, N. M. Franko, J. K. Logue, H. V. Dang, K. Hauser, J. di Iulio, W. Rivera, G. Schnell, A. Rajesh, J. Zhou, N. Farhat, H. Kaiser, M. Montiel-Ruiz, J. Noack, F. A. Lempp, J. Janer, R. Abdelnabi, P. Maes, P. Ferrari, A. Ceschi, O. Giannini, G. D. de Melo, L. Kergoat, H. Bourhy, J. Neyts, L. Soriaga, L. A. Purcell, G. Snell, S. P. J. Whelan, A. Lanzavecchia, H. W. Virgin, L. Piccoli, H. Y. Chu, M. S. Pizzuto, D. Corti and D. Veesler, Imprinted Antibody Responses against SARS-CoV-2 Omicron Sublineages, *Science*, 2022, **378**, 619–627, DOI: **10.1126/science.adc9127**.

54 N. P. Hachmann, J. Miller, A. Y. Collier, J. D. Ventura, J. Yu, M. Rowe, E. A. Bondzie, O. Powers, N. Surve, K. Hall and D. H. Barouch, Neutralization Escape by SARS-CoV-2 Omicron Subvariants BA.2.12.1, BA.4, and BA.5, *N. Engl. J. Med.*, 2022, **387**, 86–88, DOI: **10.1056/NEJMc2206576**.

55 W. Zhang, K. Shi, Q. Geng, G. Ye, H. Aihara and F. Li, Structural Basis for Mouse Receptor Recognition by SARS-CoV-2 Omicron Variant, *Proc. Natl. Acad. Sci. U.S. A.*, 2022, **119**, e2206509119, DOI: **10.1073/pnas.2206509119**.

56 C. Sun, C. Xie, G.-L. Bu, L.-Y. Zhong and M.-S. Zeng, Molecular Characteristics, Immune Evasion, and Impact of SARS-CoV-2 Variants, *Signal Transduction Targeted Ther.*, 2022, **7**, 202, DOI: **10.1038/s41392-022-01039-2**.

57 T. Sztain, S. H. Ahn, A. T. Bogetti, L. Casalino, J. A. Goldsmith, E. Seitz, R. S. McCool, F. L. Kearns, F. Acosta-Reyes, S. Maji, G. Mashayekhi, J. A. McCammon, A. Ourmazd, J. Frank, J. S. McLellan, L. T. Chong and R. E. Amaro, A glycan gate controls the opening of the SARS-CoV-2 spike protein, *Nat. Chem.*, 2021, **13**, 963–968, DOI: **10.1038/s41557-021-00758-3**.

58 M. Sikora, S. von Bülow, F. E. C. Blanc, M. Gecht, R. Covino and G. Hummer, Computational epitope map of SARS-CoV-2 spike protein, *PLoS Comput. Biol.*, 2021, **17**, e1008790, DOI: **10.1371/journal.pcbi.1008790**.

59 Y. T. Pang, A. Acharya, D. L. Lynch, A. Pavlova and J. C. Gumbart, SARS-CoV-2 Spike Opening Dynamics and Energetics Reveal the Individual Roles of Glycans and Their Collective Impact, *Commun. Biol.*, 2022, **5**, 1170, DOI: **10.1038/s42003-022-04138-6**.

60 C. Xu, Y. Wang, C. Liu, C. Zhang, W. Han, X. Hong, Y. Wang, Q. Hong, S. Wang, Q. Zhao, Y. Wang, Y. Yang, K. Chen, W. Zheng, L. Kong, F. Wang, Q. Zuo, Z. Huang and Y. Cong, Conformational dynamics of SARS-CoV-2 trimeric spike glycoprotein in complex with receptor ACE2 revealed by cryo-EM, *Sci. Adv.*, 2021, **7**, eabe5575, DOI: **10.1126/sciadv.abe5575**.

61 T. Mori, J. Jung, C. Kobayashi, H. M. Dokainish, S. Re and Y. Sugita, Elucidation of interactions regulating conformational stability and dynamics of SARS-CoV-2 S-protein, *Biophys. J.*, 2021, **120**, 1060–1071, DOI: **10.1016/j.bpj.2021.01.012**.

62 M. I. Zimmerman, J. R. Porter, M. D. Ward, S. Singh, N. Vithani, A. Meller, U. L. Mallimadugula, C. E. Kuhn, J. H. Borowsky, R. P. Wiewiora, M. F. D. Hurley, A. M. Harbison, C. A. Fogarty, J. E. Coffland, E. Fadda, V. A. Voelz, J. D. Chodera and G. R. Bowman, SARS-CoV-2 simulations go exascale to predict dramatic spike opening and cryptic pockets across the proteome, *Nat. Chem.*, 2021, **13**, 651–659, DOI: **10.1038/s41557-021-00707-0**.

63 T. Mori, J. Jung, C. Kobayashi, H. M. Dokainish, S. Re and Y. Sugita, Elucidation of Interactions Regulating Conformational Stability and Dynamics of SARS-CoV-2 S-Protein, *Biophys. J.*, 2021, **120**, 1060–1071, DOI: **10.1016/j.bpj.2021.01.012**.

64 H. M. Dokainish, S. Re, T. Mori, C. Kobayashi, J. Jung and Y. Sugita, The inherent flexibility of receptor binding domains in SARS-CoV-2 spike protein, *eLife*, 2022, **11**, e75720, DOI: **10.7554/eLife.75720**.

65 H. M. Dokainish and Y. Sugita, Structural Effects of Spike Protein D614G Mutation in SARS-CoV-2, *Biophys. J.*, 2023, **122**(14), 2910–2920, DOI: **10.1016/j.bpj.2022.11.025**.

66 G. M. Verkhivker, Coevolution, dynamics and allostery conspire in shaping cooperative binding and signal transmission of the SARS-CoV-2 spike protein with human angiotensin-converting enzyme 2, *Int. J. Mol. Sci.*, 2020, **21**, 8268, DOI: **10.3390/ijms21218268**.

67 G. M. Verkhivker, Molecular simulations and network modeling reveal an allosteric signaling in the SARS-CoV-2 spike proteins, *J. Proteome Res.*, 2020, **19**, 4587–4608, DOI: **10.1021/acs.jproteome.0c00654**.

68 G. M. Verkhivker and L. Di Paola, Dynamic Network Modeling of Allosteric Interactions and Communication Pathways in the SARS-CoV-2 Spike Trimer Mutants: Differential Modulation of Conformational Landscapes and Signal Transmission via Cascades of Regulatory Switches, *J. Phys. Chem. B*, 2021, **125**, 850–873, DOI: **10.1021/acs.jpcb.0c10637**.

69 G. M. Verkhivker and L. Di Paola, Integrated Biophysical Modeling of the SARS-CoV-2 Spike Protein Binding and Allosteric Interactions with Antibodies, *J. Phys. Chem. B*, 2021, **125**, 4596–4619, DOI: **10.1021/acs.jpcb.1c00395**.

70 G. M. Verkhivker, S. Agajanian, D. Y. Oztas and G. Gupta, Comparative Perturbation-Based Modeling of the SARS-CoV-2 Spike Protein Binding with Host Receptor and Neutralizing Antibodies: Structurally Adaptable Allosteric Communication Hotspots Define Spike Sites Targeted by Global Circulating Mutations, *Biochemistry*, 2021, **60**, 1459–1484, DOI: **10.1021/acs.biochem.1c00139**.

71 G. M. Verkhivker, S. Agajanian, D. Y. Oztas and G. Gupta, Dynamic Profiling of Binding and Allosteric Propensities of the SARS-CoV-2 Spike Protein with Different Classes of Antibodies: Mutational and Perturbation-Based Scanning Reveals the Allosteric Duality of Functionally Adaptable Hotspots, *J. Chem. Theory Comput.*, 2021, **17**, 4578–4598, DOI: **10.1021/acs.jctc.1c00372**.

72 G. M. Verkhivker, S. Agajanian, D. Y. Oztas and G. Gupta, Allosteric Control of Structural Mimicry and Mutational Escape in the SARS-CoV-2 Spike Protein Complexes with the ACE2 Decoys and Miniprotein Inhibitors: A Network-Based Approach for Mutational Profiling of Binding and Signaling, *J. Chem. Inf. Model.*, 2021, **61**, 5172–5191, DOI: **10.1021/acs.jcim.1c00766**.

73 M. L. Hossen, P. Baral, T. Sharma, B. Gerstman and P. Chapagain, Significance of the RBD mutations in the SARS-CoV-2 omicron: from spike opening to antibody escape and cell attachment, *Phys. Chem. Chem. Phys.*, 2022, **24**, 9123–9129, DOI: **10.1039/d2cp00169a**.

74 B. Jawad, P. Adhikari, R. Podgornik and W. Y. Ching, Binding Interactions between Receptor-Binding Domain of Spike Protein and Human Angiotensin Converting Enzyme-2 in Omicron Variant, *J. Phys. Chem. Lett.*, 2022, **13**, 3915–3921, DOI: **10.1021/acs.jpclett.2c00423**.

75 H. H. Gan, A. Twaddle, B. Marchand and K. C. Gunsalus, Structural Modeling of the SARS-CoV-2 Spike/Human ACE2 Complex Interface can Identify High-Affinity Variants Associated with Increased Transmissibility, *J. Mol. Biol.*, 2021, **433**, 167051, DOI: **10.1016/j.jmb.2021.167051**.

76 G. Verkhivker, S. Agajanian, R. Kassab and K. Krishnan, Computer Simulations and Network-Based Profiling of Binding and Allosteric Interactions of SARS-CoV-2 Spike Variant Complexes and the Host Receptor: Dissecting the Mechanistic Effects of the Delta and Omicron Mutations, *Int. J. Mol. Sci.*, 2022, **23**, 4376, DOI: **10.3390/ijms23084376**.

77 G. Verkhivker, S. Agajanian, R. Kassab and K. Krishnan, Probing Mechanisms of Binding and Allostery in the SARS-CoV-2 Spike Omicron Variant Complexes with the Host Receptor: Revealing Functional Roles of the Binding Hotspots in Mediating Epistatic Effects and Communication with Allosteric Pockets, *Int. J. Mol. Sci.*, 2022, **23**, 11542, DOI: **10.3390/ijms231911542**.

78 G. Verkhivker, M. Alshahrani and G. Gupta, Balancing Functional Tradeoffs between Protein Stability and ACE2 Binding in the SARS-CoV-2 Omicron BA.2, BA.2.75 and XBB Lineages: Dynamics-Based Network Models Reveal Epistatic Effects Modulating Compensatory Dynamic and Energetic Changes, *Viruses*, 2023, **15**, 1143, DOI: **10.3390/v15051143**.

79 P. W. Rose, A. Prlic, A. Altunkaya, C. Bi, A. R. Bradley, C. H. Christie, L. D. Costanzo, J. M. Duarte, S. Dutta, Z. Feng, R. K. Green, D. S. Goodsell, B. Hudson, T. Kalro, R. Lowe, E. Peisach, C. Randle, A. S. Rose, C. Shao, Y. P. Tao, Y. Valasatava, M. Voigt, J. D. Westbrook, J. Woo, H. Yang, J. Y. Young, C. Zardecki, H. M. Berman and S. K. Burley, The RCSB protein data bank: integrative view of protein, gene and 3D structural information, *Nucleic Acids Res.*, 2017, **45**, D271–D281, DOI: **10.1093/nar/gkw1000**.

80 M. L. Hekkelman, T. A. Te Beek, S. R. Pettifer, D. Thorne, T. K. Attwood and G. Vriend, WIWS: A protein structure bioinformatics web service collection, *Nucleic Acids Res.*, 2010, **38**, W719–W723, DOI: **10.1093/nar/gkq453**.

81 C. R. Søndergaard, M. H. Olsson, M. Rostkowski and J. H. Jensen, Improved treatment of ligands and coupling effects in empirical calculation and rationalization of pK_a values, *J. Chem. Theory Comput.*, 2011, **7**, 2284–2295, DOI: **10.1021/ct200133y**.

82 M. H. Olsson, C. R. Søndergaard, M. Rostkowski and J. H. Jensen, PROPKA3: consistent treatment of internal and surface residues in empirical pK_a predictions, *J. Chem. Theory Comput.*, 2011, **7**, 525–537, DOI: **10.1021/ct100578z**.

83 N. Fernandez-Fuentes, J. Zhai and A. Fiser, ArchPRED: A template based loop structure prediction server, *Nucleic Acids Res.*, 2006, **34**, W173–W176, DOI: **10.1093/nar/gkl113**.

84 G. G. Krivov, M. V. Shapovalov and R. L. Dunbrack, Improved prediction of protein side-chain conformations with SCWRL4, *Proteins*, 2009, **77**, 778–795, DOI: **10.1002/prot.22488**.

85 D. Bhattacharya, J. Nowotny, R. Cao and J. Cheng, 3Drefine: An Interactive Web Server for Efficient Protein Structure Refinement, *Nucleic Acids Res.*, 2016, **44**, W406–W409, DOI: **10.1093/nar/gkw336**.

86 J. Huang, S. Rauscher, G. Nawrocki, T. Ran, M. Feig, B. L. de Groot, H. Grubmüller and A. D. MacKerell, Jr., CHARMM36m: an improved force field for folded and intrinsically disordered proteins, *Nat. Methods*, 2017, **14**, 71–73, DOI: **10.1038/nmeth.4067**.

87 W. L. Jorgensen, J. Chandrasekhar, J. D. Madura, R. W. Impey and M. L. Klein, Comparison of Simple Potential Functions for Simulating Liquid Water, *J. Chem. Phys.*, 1983, **79**, 926–935, DOI: **10.1063/1.445869**.

88 H. S. Fernandes, S. F. Sousa and N. M. F. S. A. Cerqueira, VMD Store-A VMD Plugin to Browse, Discover, and Install VMD Extensions, *J. Chem. Inf. Model.*, 2019, **59**, 4519–4523, DOI: **10.1021/acs.jcim.9b00739**.

89 M. C. Childers and V. Daggett, Validating Molecular Dynamics Simulations against Experimental Observables in Light of Underlying Conformational Ensembles, *J. Phys. Chem. B*, 2018, **122**, 6673–6689, DOI: **10.1021/acs.jpcb.8b02144**.

90 J.-P. Ryckaert, G. Ciccotti and H. J. C. Berendsen, Numerical Integration of the Cartesian Equations of Motion of a System with Constraints: Molecular Dynamics of n-Alkanes, *J. Comput. Phys.*, 1977, **23**, 327–341, DOI: **10.1016/0021-9991(77)90098-5**.

91 M. Di Pierro, R. Elber and B. Leimkuhler, A Stochastic Algorithm for the Isobaric-Isothermal Ensemble with Ewald Summations for All Long Range Forces, *J. Chem. Theory Comput.*, 2015, **11**, 5624–5637, DOI: **10.1021/acs.jctc.5b00648**.

92 P. Eastman, J. Swails, J. D. Chodera, R. T. McGibbon, Y. Zhao, K. A. Beauchamp, L.-P. Wang, A. C. Simmonett,

M. P. Harrigan, C. D. Stern, R. P. Wiewiora, B. R. Brooks and V. S. Pande, OpenMM 7: Rapid Development of High Performance Algorithms for Molecular Dynamics, *PLoS Comput. Biol.*, 2017, **13**, e1005659, DOI: **10.1371/journal.pcbi.1005659**.

93 R. T. McGibbon, K. A. Beauchamp, M. P. Harrigan, C. Klein, J. M. Swails, C. X. Hernández, C. R. Schwantes, L.-P. Wang, T. J. Lane and V. S. Pande, MDTraj: A Modern Open Library for the Analysis of Molecular Dynamics Trajectories, *Biophys. J.*, 2015, **109**, 1528–1532, DOI: **10.1016/j.bpj.2015.08.015**.

94 I. S. Haque, K. A. Beauchamp and V. S. Pande, *N*, *bioRxiv*, 2014 , DOI: **10.1101/008631**.

95 D. L. Theobald, Rapid Calculation of RMSDs Using a Quaternion-Based Characteristic Polynomial, *Acta Crystallogr., Sect. A: Found. Crystallogr.*, 2005, **61**, 478–480.

96 P. Liu, D. K. Agrafiotis and D. L. Theobald, Fast Determination of the Optimal Rotational Matrix for Macromolecular Superpositions, *J. Comput. Chem.*, 2010, **31**, 1561–1563, DOI: **10.1002/jcc.21439**.

97 D. K. Brown, D. L. Penkler, O. Sheik Amamuddy, C. Ross, A. R. Atilgan, C. Atilgan and Ö. Tastan Bishop, MD-TASK: A Software Suite for Analyzing Molecular Dynamics Trajectories, *Bioinformatics*, 2017, **33**, 2768–2771, DOI: **10.1093/bioinformatics/btx349**.

98 Y. Dehouck, J. M. Kwasigroch, M. Rooman and D. Gilis, BeAtMuSiC: Prediction of changes in protein-protein binding affinity on mutations, *Nucleic Acids Res.*, 2013, **41**, W333–W339, DOI: **10.1093/nar/gkt450**.

99 W. Kabsch and C. Sander, Dictionary of Protein Secondary Structure: Pattern Recognition of Hydrogen-Bonded and Geometrical Features, *Biopolymers*, 1983, **22**, 2577–2637, DOI: **10.1002/bip.360221211**.

100 C. Atilgan and A. R. Atilgan, Perturbation-response scanning reveals ligand entry-exit mechanisms of ferric binding protein, *PLoS Comput. Biol.*, 2009, **5**, e1000544.

101 C. Atilgan, Z. N. Gerek, S. B. Ozkan and A. R. Atilgan, Manipulation of conformational change in proteins by single-residue perturbations, *Biophys. J.*, 2010, **99**, 933–943.

102 F. Jalalypour, O. Sensoy and C. Atilgan, Perturb-Scan-Pull: A Novel Method Facilitating Conformational Transitions in Proteins, *J. Chem. Theory Comput.*, 2020, **16**, 3825–3841.

103 S. Zhang, J. M. Krieger, Y. Zhang, C. Kaya, B. Kaynak, K. Mikulska-Ruminska, P. Doruker, H. Li and I. Bahar, ProDy 2.0: Increased Scale and Scope after 10 Years of Protein Dynamics Modelling with Python, *Bioinformatics*, 2021, **37**, 3657–3659, DOI: **10.1093/bioinformatics/btab187**.

104 I. J. General, Y. Liu, M. E. Blackburn, W. Mao, L. M. Gierasch and I. Bahar, ATPase subdomain IA is a mediator of interdomain allostery in Hsp70 molecular chaperones, *PLoS Comput. Biol.*, 2014, **10**, e1003624.

105 A. Dutta, J. Krieger, J. Y. Lee, J. Garcia-Nafria, I. H. Greger and I. Bahar, Cooperative Dynamics of Intact AMPA and NMDA Glutamate Receptors: Similarities and Subfamily-Specific Differences, *Structure*, 2015, **23**, 1692–1704.

106 G. M. Verkhivker and L. Di Paola, Dynamic Network Modeling of Allosteric Interactions and Communication Pathways in the SARS-CoV-2 Spike Trimer Mutants: Differential Modulation of Conformational Landscapes and Signal Transmission via Cascades of Regulatory Switches, *J. Phys. Chem. B*, 2021, **125**, 850–873.

107 K. V. Brinda and S. Vishveshwara, A network representation of protein structures: implications for protein stability, *Biophys. J.*, 2005, **89**, 4159–4170.

108 M. S. Vijayabaskar and S. Vishveshwara, Interaction energy based protein structure networks, *Biophys. J.*, 2010, **99**, 3704–3715.

109 A. Sethi, J. Eargle, A. A. Black and Z. Luthey-Schulten, Dynamical networks in tRNA:protein complexes, *Proc. Natl. Acad. Sci. U. S. A.*, 2009, **106**, 6620–6625.

110 G. Stetz and G. M. Verkhivker, Computational analysis of residue interaction networks and coevolutionary relationships in the Hsp70 chaperones: a community-hopping model of allosteric regulation and communication, *PLoS Comput. Biol.*, 2017, **13**, e1005299.

111 A. J. M. Martin, M. Vidotto, F. Boscariol, T. Di Domenico, I. Walsh and S. C. E. Tosatto, RING: Networking Interacting Residues, Evolutionary Information and Energetics in Protein Structures, *Bioinformatics*, 2011, **27**, 2003–2005, DOI: **10.1093/bioinformatics/btr191**.

112 A. Del Conte, A. M. Monzon, D. Clementel, G. F. Camagni, G. Minervini, S. C. E. Tosatto and D. Piovesan, RING-PyMOL: Residue Interaction Networks of Structural Ensembles and Molecular Dynamics Bioinformatics, *Bioinformatics*, 2023, **39**, btad260, DOI: **10.1093/bioinformatics/btad260**.

113 D. Clementel, A. Del Conte, A. M. Monzon, G. F. Camagni, G. Minervini, D. Piovesan and S. C. E. Tosatto, RING 3.0: Fast Generation of Probabilistic Residue Interaction Networks from Structural Ensembles, *Nucleic Acids Res.*, 2022, **50**, W651–W656, DOI: **10.1093/nar/gkac365**.

114 A. A. Hagberg, D. A. Schult and P. J. Swart, Exploring network structure, dynamics, and function using NetworkX, in *Proceedings of the 7th Python in Science Conference (SciPy2008), Pasadena, CA, USA, 19–24 August 2008*, ed. G. Varoquaux, T. Vaught and J. Millman, Scientific Research, Atlanta, GA, USA, 2011, pp. 11–15.

115 A. del Sol, H. Fujihashi, D. Amoros and R. Nussinov, Residues crucial for maintaining short paths in network communication mediate signaling in proteins, *Mol. Syst. Biol.*, 2006, **2**, 2006.0019, DOI: **10.1038/msb4100063**.

116 G. Brysbaert, T. Mauri and M. F. Lensink, Comparing protein structures with RINspector automation in Cytoscape, *F1000Res.*, 2018, **7**, 563, DOI: **10.12688/f1000research.14298.2**.

117 A. Rössler, A. Netzl, L. Knabl, H. Schäfer, S. H. Wilks, D. Bante, B. Falkensammer, W. Borena, D. von Laer and D. J. Smith, Kimpel, J. BA.2 and BA.5 Omicron Differ Immunologically from Both BA.1 Omicron and Pre-Omicron Variants, *Nat. Commun.*, 2022, **13**, 7701, DOI: **10.1038/s41467-022-35312-3**.

118 D. F. A. R. Dourado and S. C. Flores, A Multiscale Approach to Predicting Affinity Changes in Protein-Protein

Interfaces, *Proteins*, 2014, **82**, 2681–2690, DOI: **10.1002/prot.24634**.

119 A. Meseguer, L. Dominguez, P. M. Bota, J. Aguirre-Plans, J. Bonet, N. Fernandez-Fuentes and B. Oliva, Using Collections of Structural Models to Predict Changes of Binding Affinity Caused by Mutations in Protein–Protein Interactions, *Protein Sci.*, 2020, **29**, 2112–2130, DOI: **10.1002/pro.3930**.

120 J. Van Durme, J. Delgado, F. Stricher, L. Serrano, J. Schymkowitz and F. Rousseau, A Graphical Interface for the FoldX Force Field, *Bioinformatics*, 2011, **27**, 1711–1712.

121 R. F. Alford, A. Leaver-Fay, J. R. Jeliazkov, M. J. O'Meara, F. P. DiMaio, H. Park, M. V. Shapovalov, P. D. Renfrew, V. K. Mulligan, K. Kappel, J. W. Labonte, M. S. Pacella, R. Bonneau, P. Bradley, R. L. Dunbrack, R. Das, D. Baker, B. Kuhlman, T. Kortemme and J. J. Gray, The Rosetta All-Atom Energy Function for Macromolecular Modeling and Design, *J. Chem. Theory Comput.*, 2017, **13**, 3031–3048, DOI: **10.1021/acs.jctc.7b00125**.

122 T. N. Starr, A. J. Greaney, S. K. Hilton, D. Ellis, K. H. D. Crawford, A. S. Dingens, M. J. Navarro, J. E. Bowen, M. A. Tortorici, A. C. Walls, N. P. King, D. Veesler and J. D. Bloom, Deep Mutational Scanning of SARS-CoV-2 Receptor Binding Domain Reveals Constraints on Folding and ACE2 Binding, *Cell*, 2020, **182**, 1295–1310.e20, DOI: **10.1016/j.cell.2020.08.012**.

123 T. N. Starr, A. J. Greaney, C. M. Stewart, A. C. Walls, W. W. Hannon, D. Veesler and J. D. Bloom, Deep Mutational Scans for ACE2 Binding, RBD Expression, and Antibody Escape in the SARS-CoV-2 Omicron BA.1 and BA.2 Receptor-Binding Domains, *PLoS Pathog.*, 2022, **18**, e1010951, DOI: **10.1371/journal.ppat.1010951**.

124 T. N. Starr, A. J. Greaney, W. W. Hannon, A. N. Loes, K. Hauser, J. R. Dillen, E. Ferri, A. G. Farrell, B. Dadonaite, M. McCallum, K. A. Matreyek, D. Corti, D. Veesler, G. Snell and J. D. Bloom, Shifting mutational constraints in the SARS-CoV-2 receptor-binding domain during viral evolution, *Science*, 2022, **377**, 420–424, DOI: **10.1126/science.abo7896**.

125 A. Moulana, T. Dupic, A. M. Phillips, J. Chang, S. Nieves, A. A. Roffler, A. J. Greaney, T. N. Starr, J. D. Bloom and M. M. Desai, Compensatory Epistasis Maintains ACE2 Affinity in SARS-CoV-2 Omicron BA.1, *Nat. Commun.*, 2022, **13**, 7011, DOI: **10.1038/s41467-022-34506-z**.

126 J. Zahradník, S. Marciano, M. Shemesh, E. Zoler, D. Harari, J. Chiaravalli, B. Meyer, Y. Rudich, C. Li, I. Marton, O. Dym, N. Elad, M. G. Lewis, H. Andersen, M. Gagne, R. A. Seder, D. C. Douek and G. Schreiber, SARS-CoV-2 Variant Prediction and Antiviral Drug Design Are Enabled by RBD in Vitro Evolution, *Nat. Microbiol.*, 2021, **6**, 1188–1198, DOI: **10.1038/s41564-021-00954-4**.

127 C. Sun, Y.-F. Kang, Y.-T. Liu, X.-W. Kong, H.-Q. Xu, D. Xiong, C. Xie, Y.-H. Liu, S. Peng, G.-K. Feng, Z. Liu and M.-S. Zeng, Parallel Profiling of Antigenicity Alteration and Immune Escape of SARS-CoV-2 Omicron and Other Variants, *Signal Transduct. Target Ther.*, 2022, **7**, 42, DOI: **10.1038/s41392-022-00910-6**.

128 A. M. Carabelli, T. P. Peacock, L. G. Thorne, W. T. Harvey, J. Hughes, COVID-19 Genomics UK Consortium, T. I. de Silva, S. J. Peacock, W. S. Barclay, T. I. de Silva, G. J. Towers and D. L. Robertson, SARS-CoV-2 Variant Biology: Immune Escape, Transmission and Fitness, *Nat. Rev. Microbiol.*, 2023, **21**, 162–177, DOI: **10.1038/s41579-022-00841-7**.

